Chapter 5

Interaction Region

5.1 Overview

The energy asymmetry of the two beams shifts the interaction point (IP) of SuperKEKB by 471 mm from the geometrical center of Belle II detector. The direction, towards which the center of mass system of colliding particles is boosted, is called 'Forward direction' or 'Right hand side' of the IP. The other side is called 'Backward direction' or 'Left hand side'. Figure 5.1 is a plane view of the layout of the detector, magnets and beam pipes around the IP. The right hand side of the figure is the forward direction.

The orbits cross with an angle of 83 mrad at the IP. The location of final focus magnets is very close to the IP as listed in Table 5.1. These are superconducting magnets. At both sides of the IP, these final focus magnets of each ring are integrated with compensation solenoids for the detector solenoid field, correctors, cancel coils against leak fields, magnetic yokes to absorb leak fields, and heavy metal radiation shields, in a single cryostat. This integrated set is called QCSL in the backward, and QCSR in the forward, and they are collectively referred as QCS. The fabrication of QCS with required precision is one of the most challenging issues in the upgrade.

The body of the cryostat of QCS is buried within the Belle II detector. QCS's are aligned first without the detector. Then the detector rolls in. QCS's have to temporally move away from their original position and come back after the roll-in. Therefore, QCS is supported on a moving stage. The motion of this moving stage must reproduce the aligned position of QCS very precisely. And, the stage must stand for a very strong force on QCS exerted by the detector solenoid at the final position. After QCS reaches the final position within the detector, the 'Single Stretched Wire' technique is applied to measure the magnetic centers of the final focus quadrupole magnets with respect to the design beam lines. In the detector, the transversal shift of the QCS is monitored

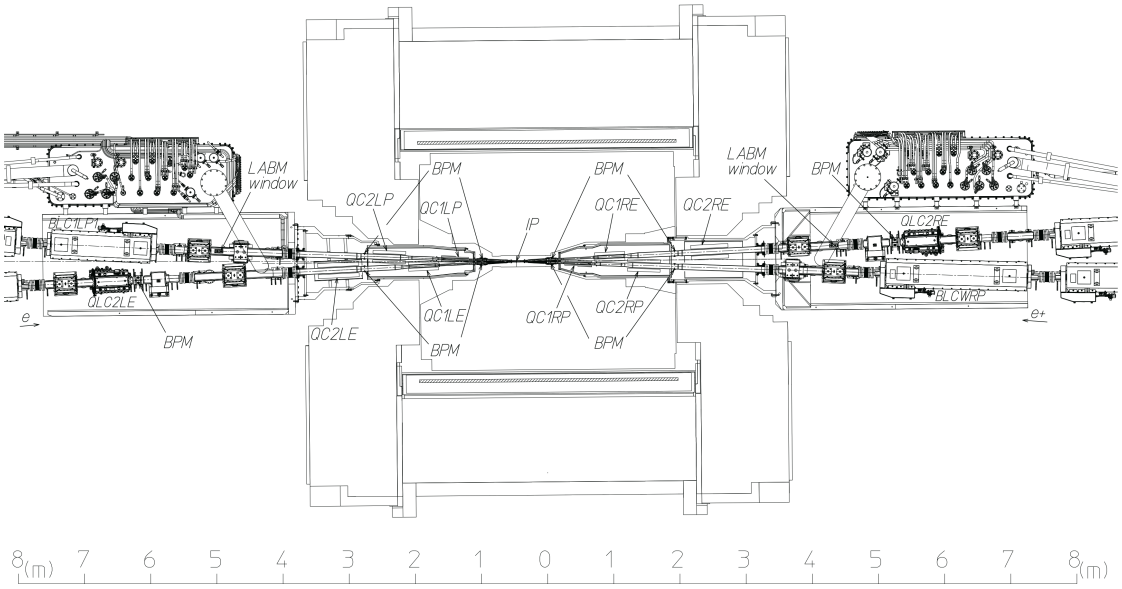

Figure 5.1: A sketch of an area ±8 m from the IP.

	Incoming beam	Distance [m]	Outgoing beam	Distance [m]
Positron	QC1RP	0.935	QC1LP	0.935
	QC2RP	1.925	QC2LP	1.925
Electron	QC1LE	1.41	QC1RE	1.41
	QC2LE	2.70	QC2RE	2.925

Table 5.1: Distance of final focus magnets from the IP.

with a gap-sensor set between the cryostat and the surrounding central drift chamber.

The exit of the final bend of LER is about 5.54 m from the IP, the critical energy of synchrotron radiation (SR) from this bend is 0.95 keV. The end of the final bend of HER is at about 7.26 m and its critical energy is 1.25 keV. The curvature of the orbit in these magnets is designed to avoid direct illumination of SR on the central beryllium pipe of the IP chamber (see below). The detail of the moving stage and compact room temperature magnets in this region will be described in the magnet section.

The central beam pipe (IP chamber) has a short beryllium tube in the middle. The length of the IP chamber is 964 mm. Two rings separate within the IP chamber. The IP chamber is connected to a short tube with a bellows unit and a beam position monitor (BPM). This bellows unit has a finger-type RF-bridge like the one used for KEKB. We cannot apply the comb-type RF-bridge (see chapter of the vacuum system), because a flexible design for a small diameter such as 20 mm is not possible with the

	IP	IP1	IP2	QC1LP	QC1LE	QC2LP	QC2LE	Outside
Electron incoming	20	10	20	(21)	34	(70)	80	80
Positron outgoing	20	20	20	27(V) 21(H)	(44)	70	(80)	80
	IP	IP1	IP2	QC1RP	QC1RE	QC2RP	QC2RE	Outside
Electron outgoing	20	20	20	(21)	34	(70)	80	80
Positron incoming	20	10	20	27(V) 21(H)	(44)	70	(80)	80

Table 5.2: Diameter of beam pipes (mm). The cross section is circular except at QC1RP and QC1LP. IP1 is the position where two beams separate. For an outgoing beam, the beam pipe has a horizontal off-set at IP1. IP2 is the end of the IP chamber.

comb-type ridge. This RF-bridge must withstand a three times higher wall current than the one experienced at KEKB. The next vacuum chamber is used both as beam pipe and warm bore of the cryostat to locate the final focus magnets as close to the IP as possible. By this design we have vacuum flange connections in front of the cryostat, which is not attainable from behind. Physical aperture of beam pipes from IP to the end of QCS is summarized in Table 5.2.

The BPM nearest to IP is located between the IP chamber and the QCS cryostat. They are on a short beam pipe with bellows as mentioned above. These BPM's are mechanically fixed to the IP chamber. The next BPM is located in the cryostat. For HER the position is between QC1 and QC2, however, it is after QC2 for LER. The third location of HER BPM is at the quadrupole magnet next to the cryostat. However, for LER, the third BPM is beyond two bending magnets from the cryostat.

Mirrors and windows for the large angle beam-strahlung monitor (LABM) system are provided on the beam pipe for outgoing beam after the cryostat. The distance from IP is about 4.5 m for LER and 4.8 m for HER. The detail of this monitoring system will be described in the chapter of the beam monitor system.

The luminosity monitor in the positron beam line will be installed about 7 m downstream of IP. A signal of positrons whose energy is lost by the radiative Bhabha process at the interaction point is used as a measure of the luminosity. The location for HER is not yet fixed. This beam loss due to the radiative Bhabha process is a major radiation source in the interaction region.

5.2 Final focus superconducting magnet system (QCS)

5.2.1 General configuration of the system

The superconducting magnet system was designed in order to control the beam conditions at the beam interaction point, IP [1]. In the design of the system, the following constraints are required from the beam optics and the particle detectors: (1) While we need to keep the same boundaries to the detector components as KEKB, the superconducting magnets must be located closer to IP than KEKB to squeeze a vertical beam size to around 50 nm at IP. (2) From the requirement of locating the magnets in the space of the small beam separation between two beam lines of LER and HER, the magnet components including the conductor sizes of the superconducting coils are required to be optimized. (3) Since the beta functions for these magnets are so large, 1200 m for horizontal and 6400 m for vertical, a larger space with a good field quality is required. (4) These magnets must apply the focusing fields on electrons and positrons, independently each other. So, the reduction of the non-linear leakage field from the adjacent beam lines is a critical issue to achieve large dynamic aperture. (5) Since two beams with the crossing angle of 83 mrad are operated under the Belle-II solenoid field at 1.5 T [2], the solenoid field is required to be cancelled integrally along each beam line. The compensation solenoids [3] are designed to reduce the X-Y coupling and the emittance for the two beams.

Figure 5.2 shows the designed final focus magnet cryostat system in the Belle-II detector. The system consists of 8 main quadrupole magnets, 4 compensation solenoids, 35 corrector magnets and 8 special magnets [4][5]to cancel the leakage magnetic fields on the HER beam lines from QC1LP/RP. The main quadrupole magnets (QC1s and QC2s) are designed to form a quadrupole doublet for each beam, as shown in Fig. 5.3.

Table 5.3 shows the main parameters of the quadrupole magnets at the colliding energy of 11 GeV of the nominal operation. In the table, the integral field gradients are shown with the field gradients at the magnet center and the magnetic length. The mid-planes of the quadrupole fields of the LER magnets roll with the angles as shown in the table. The QC1LP/RP magnets are located at the closest position, +/- 935 mm, to IP. They are the quadrupole magnets without magnetic yokes in order to superimpose the fields of the compensation solenoids on the Belle II solenoid field in this area and make the solenoid field profile for minimizing vertical beam emittance. The QC1RE/LE and QC2RP/LP magnets have the Permendur yokes. The QC2RE/LE magnets have the iron yokes. The distances of the quadrupole centers from IP and the mid-plane angles to the horizontal plane are listed in the table. The quadrupole magnets for LER are assembled with these angles in the cryostats.

Table 5.3: Main Quadrupole Parameters

Magnet	GL, T (T/m × m)	Type	Z, mm	θ, mrad
QC2RE	13.58 (32.41 × 0.419)	Yoked	2925	0
QC2RP	11.56 (26.28 × 0.410)	Yoked	1925	-2.114
QC1RE	26.45 (70.89 × 0.373)	Yoked	1410	0
QC1RP	22.98 (68.89 × 0.334)	no Yoke	935	7.204
QC1LP	22.97 (68.94 × 0.334)	no Yoke	-935	-13.65
QC1LE	26.94 (72.21 × 0.373)	Yoked	-1410	0
QC2LP	11.50 (28.44 × 0.410)	Yoked	-1925	-3.725
QC2LE	15.27 (28.44 × 0.537)	Yoked	-2700	0

Since the solenoid field and the leakage field of QC1P magnets change the e^- beam orbits, the beam orbits will be controlled by dipole corrector magnets. In order to minimize the required magnetic fields of the corrector magnets, the magnet axes of QC1s and QC2s are shifted as shown in Table 5.4. In the table, ΔY is the shift amount in vertical direction from the horizontal plane including IP and the negative sign means downward. The plus ΔX means the horizontal shift toward the outer direction of the accelerator ring.

Since the QC1LP/RP magnets are non-yoked magnets, the leakage field from the magnets to the e- beam line contains all field components as shown in Fig. 5.4. In the figure, the horizontal axis corresponds to the distance from IP on the HER beam line. In order to cancel these field components, the B_3, B_4, B_5 and B_6 cancel magnets are wound on the coil bobbins as the helium inner vessel. The cancel magnets are designed to have a small twist in the windings for cancelling the skew field component which is contained in the leakage field. The B_1 and B_2 field components are included in the optics design, and then the B_1 and B_2 cancel magnets are not incorporated in the system.

The compensation solenoids, ESL, ESR1, ESR2 and ESR3, are designed to cancel the Belle-II solenoid field integrally along the beam lines. In the ESL and ESR1 solenoids, two or three quadrupoles are assembled, respectively, as shown in Figs. 5.2 and 5.3. In the right cryostat, the additional solenoids, ESR2 and ESR3, are also installed.

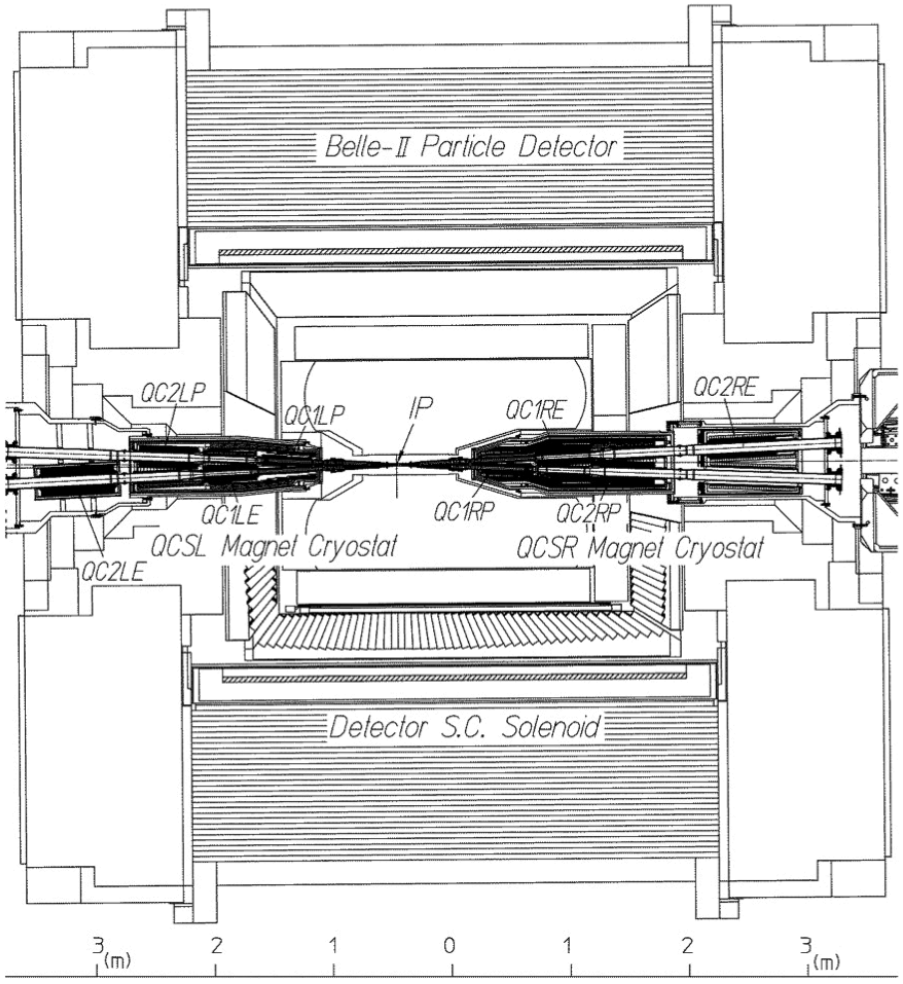

Figure 5.2: The final focus magnet-cryostat system in the Belle-II detector.

5.2.2 Superconducting quadrupole magnet design

The four cross sections of the quadrupole magnets are shown in Fig. 5.5. The magnet designs are different in order to accommodate the change of the beam pipe diameters in the cryostats. Table 5.5 shows the design parameters of the magnets. The parameters are listed as the maximum operation points when the colliding energy of 12 GeV. The magnets consist of two layer coils by the double pancake technique, and the cables are same specification except for the keystone angle.

QC1P magnet design

The QC1P magnets are designed without iron yokes because in the location of the magnets the solenoid fields by ESL and ESR1 integrally cancel the Belle-II solenoid field. The four superconducting coils are clamped with the YUS-130S stainless steel

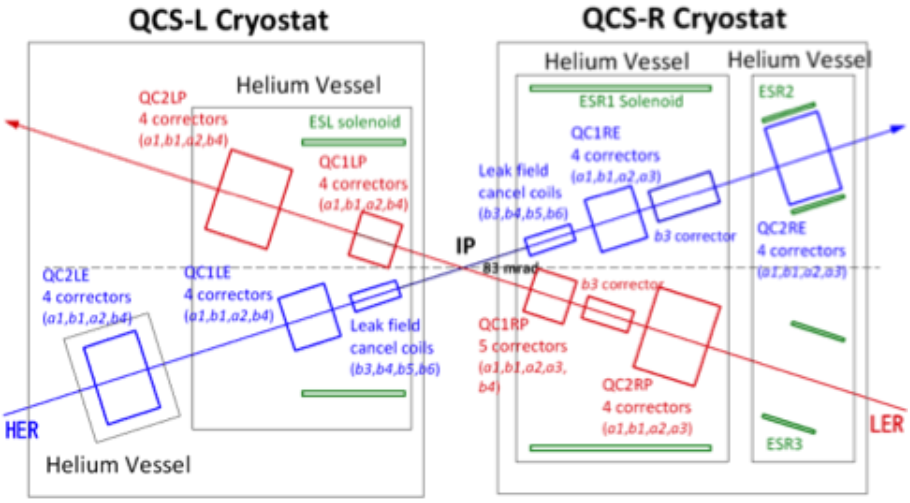

Figure 5.3: Superconducting magnet configuration in the interaction region of SuperKEKB.

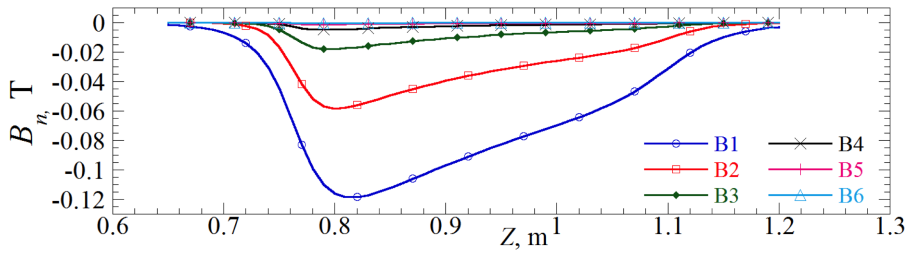

Figure 5.4: Leakage field profiles from QC1P magnet along the e- beam line.

collars. The design field gradient at the magnet center is 76.4 T/m at the current of 1800 A, and the effective magnetic length is 0.3336 m. The operating point with respect to the critical point of the superconductor is 72 % at 4.7 K. The inner radius of the QC1P magnet is 25 mm, and the physical magnet length is 409.3 mm. The QC1P magnets are very small magnets. Three corrector magnets of a_1, b_1 and a_2 are assembled inside of the magnet bore. The three corrector magnets are directly wound on the support bobbin, which has the function of the helium vessel. The b_4 corrector magnet for the QC1LP and the b_4 and a_3 corrector magnets for the QC1RP are assembled on the outer periphery of the stacked collars.

The field quality is designed on the reference radius, R_r, of 10 mm in the magnet bore. The calculated multipole field components up to the 20-th pole (n=10) are listed in Table 5.6. The multipole field components are described by the following equations,

$$B_y + iB_x = 10^{-4} B_2 \sum_{n=1}^{\infty} (b_n + ia_n) \left(\frac{x+iy}{R_{ref}} \right)^{n-1}, \tag{5.1}$$

Table 5.4: Shift amount of magnet axis.

Magnet	ΔY	Magnet	ΔY
QC1RP	-1.0 mm	QC1RE	-0.7 mm
QC2RP	-1.0 mm	QC2RE	-0.7 mm
QC1LP	-1.5 mm	QC1LE	+0.7 mm
QC2LP	-1.5 mm	QC2LE	+0.7 mm

where b_n and a_n are the normalized multipole field components as B_2 (quadrupole field amplitude value), and they are the coefficients of the normal and the skew field components (units).

The higher order multipole field components are optimized with the magnet cross sections (in 2 D model) and the whole magnet models (in 3D model), in which the magnet both ends are included. From the symmetry configuration of the four coils, the error field of the non-listed multipole numbers are 0.

Because the higher order multipole field profile along the magnet length is important for the beam optics, the profiles of the field components are calculated and they are included in the optics model. The multipole field profiles are shown in the Fig. 5.6, with the coil geometries of two layers. The field components are normalized by the quadrupole field at the magnet center as 10000. In order to exclude the skew quadrupole components in the coil lead end, the quadrant coils have mirror symmetry to the neighbor coils, while b_{4n} components are induced. In the lead ends, the b_4 components show the peaks of +25.0/-26.0 units.

The magnetic field by the QC1P magnet goes through the e^- beam line, which is the counter beam line, because this magnet does not have a magnetic yoke. The magnetic field is expanded into the multipole field components, and the profiles of the components are shown in Fig. 5.4. In order to remove the influence of the QC1P magnetic field on the operation of the electron beam, the cancel system of the leak field, which consists of twisted b_3, b_4, b_5 and b_6 magnets, is designed. These magnets ae described in the section of the superconducting corrector magnet.

QC1E magnet design

The QC1E magnets locate on the e^- beam line behind the QC1P magnets from IP. The design field gradient at the magnet center is 91.6 T/m at the current of 2000 A, and the magnetic length is 0.3731 m. The design operating point to the superconductor limit is 73 % at 4.7 K. The inner radius of the magnet is 33 mm, and the physical magnet

length is 455.4 mm. The QC1E magnets have the magnetic yokes, and the material is Permendur, which has the saturated magnetization, Ms, of 2.3 T in order to avoid magnetic saturation in the yokes due to local imperfection in cancelling Belle-II field by ESL and ESR1. Especially, in the front part of the magnet, the inner helium vessel for the positron beam line has an interference with the magnetic yokes of the QC1E magnets, and therefore some yokes are gouged.

The higher order multipole field components have been calculated with the 2D cross section, and they are listed in Table 5.6. The largest component at R_r of 15 mm is b_{10} of -0.34 units. The whole magnet field quality was calculated as same as QC1P. The designed coil ends are shown in Fig. 5.6 with the profiles of the multipole field components. The multipole field components of the whole magnet are listed in Table 5.6, and the amplitudes of them are to be smaller than 0.5 units.

Figure 5.7 shows the leak field into the positron beam line from QC1LE magnet. The magnet current is 1577 A at the 4S physics operation. In the yoke and the magnetic shield, the magnetic field is assumed to be 1 T. The upper plot shows the calculated magnetic profile in the positron beam line in case of the iron yoke of QC1LE and the iron magnetic shield, and the magnetic field strength from 0 to 0.007 T is shown with the contour lines. The lower plot is the calculated result in case of Permendur for the yoke and the magnetic shield. The magnetic field strength in the positron beam line is from 0 to 0.00035 T. By using Permendur as material of the yokes and the magnetic shields, the leak field to the e^+ beam line is reduced to the twentieth part of the field with iron.

The QC1E magnets have the 4 correctors inside of each magnet bore. The QC1LE magnet has the a_1, b_1, a_2 and b_4 corrector magnets, and the QC1RE magnet has the a_1, b_1, a_2 and a_3 corrector magnets.

QC2P, QC2LE/RE magnet designs

The inner and outer coil radii of the QC2P are 53.8 mm and 59.2 mm, respectively. The four coils are cramped with the YUS130S collars, and Permendur yokes are assembled on the collars. With the yokes, the leak field from QC2P to the e- beam line can be reduced from 50 Gauss to 2 Gauss for the magnetic field of 1 T in the yokes in case of 1 % imperfection of cancelling the detector solenoid field by ESL or ESR1. The design field gradient of QC2P at 1000 A is 32.0 T/m, and the magnetic length is 409.9 mm. The nominal operation currents of QC2LP and QC2RP are 877.4 A and 882.1 A, respectively.

The cross section designs of the QC2LE and QC2RE magnets are different while the collared coils of QC2LE and QC2RE are the same design. QC2RE has the com-

pensation solenoid between the collars and the yokes, as shown in Fig. 5.5. The inner and outer coil radii of QC2E are 59.3 mm and 64.7 mm, respectively. The material of the yokes for QC2LE and QC2RE is iron because the amount of iron in the beam separation is sufficient to reduce the leakage field to the e+ beam line to almost zero. The design field gradients of QC2LE and QC2RE are 35.3 T/m and 38.1 T/m with the currents of 1250 A and 1350 A, respectively, and the magnetic lengths are 537 mm and 419 mm, respectively. The nominal operation currents of QC2LE and QC2RE are 1007 A and 1312.8 A, respectively. From the low background noise requirement by the Belle-II detector, the QC2LE magnet is designed to be operated with the lower quadrupole field than the QC2RE magnet, and then QC2LE is physically longer than QC2RE.

The calculated multipole field components with the 2D cross sections and with the 3D models are listed in Table 5.6. The field qualities of QC2P and QC2E are designed at R_r of 30 mm and 35 mm, respectively. Under the space constraint in the cryostat, the coil ends are designed to be as short as possible, as shown in Fig. 5.8. The coil ends of QC2P and QC2E are designed within the space of 51.6 mm and 57.5 mm including the G-10 spacers, respectively. In Fig. 5.8, the field profiles along the magnet lengths of QC2P and QC2LE are shown, too. In the lead ends, the b_4 components show the peaks of +7.0/-5.0 units for QC2P and +6.0/-6.6 units for QC2LE. The integral b_4 components of QC2P and QC2LE were controlled at -0.06 units and 0.07 units, respectively, as shown in Table 5.6. The maximum error field components are b_{10}, and they are -1.43 units and -1.92 units for QC2P and QC2LE, respectively.

The QC2P magnets and the QC2LE/RE magnets have the 4 correctors inside of the magnet bore. The QC2LP and QC2LE magnets have the a_1, b_1, a_2 and b_4 corrector magnets, and the QC2RP and the QC2RE magnets have the a_1, b_1, a_2 and a_3 corrector magnets.

5.2.3 Superconducting corrector magnet design

The 43 superconducting corrector magnets including the leak field cancel magnets for the QC1P magnets are installed into the two cryostats. A few millimetres of radial space is available for corrector coils atop support bobbins that serve as the inner cold mass containment wall and the main quadrupole coils' inner surface. The correctors are directly wound on the support bobbins [6], and the productions of the correctors are performed by the superconducting magnet division of the Brookhaven National Laboratory under the US-Japan research collaboration. The corrector requirements evolved in response to results from optics optimization and tracking studies are summarized in Table 5.7, and A_n and B_n are the skew and normal correctors, respectively. The A_1

Table 5.5: Design Parameters of QC1 and QC2 Magnets.

	QC1P	**QC1E**	**QC2P**	**QC2LE/RE**
Field gradient at I_d, G, T/m	76.4	91.6	32.0	35.3/38.1
Design current, I_d, A	1800	2000	1000	1250/1350
Peak field in coil winding, T	4.56	3.50	2.43	2.63/2.84
Magnetic yoke	No	Permendur	Permendur	Iron
Coil I.R., mm	25.0	33.0	53.8	59.3
Coil O.R., mm	30.49	38.49	59.29	64.79
Collar or Yoke O.R., mm	35.5	70	93	115
Turns in a pole	25	34	54	58
Magnetic length, mm	333.6	373.1	409.9	537/419
Inductance, mH	0.88	2.19	7.32	13.28/10.36
Physical magnet length, mm	409.3	455.4	495.5	618.9/560.9
I_d /I_c, %	72	73	47	50/49
S.C. Cable	NbTi Rutherford cable, 10 strands, ϕ0.5mm of strand			
Cable size in bare, mm	2.5 in height and 0.93 in mid-thickness			
Cable size with insulation, mm	2.65 in height and 1.08 in mid-thickness			
Cable keystone angle, degree	2.14	1.66	1.05	0.94
Critical current at 5T and 4.22 K	3160	3080	3070	3130

Table 5.6: Error field components of QC1 and QC2 Magnets.

	QC1P		QC1E		QC2P		QC2 LE/RE	
Ref. radius, mm	10		15		30		35	
	an	bn	an	bn	an	bn	an	bn
2D cal. n=2	0	10000	0	10000	0	10000	0	10000
6	0	0.10	0	-0.06	0	0.00	0	-0.24
10	0	-0.21	0	-0.34	0	-0.15	0	-0.14
3D cal. n=2	0	10000	0	10000	0	10000	0	10000
4	0	0.24	0	-0.02	0	-0.06	0	0.05/0.07
6	0	0.54	0	-0.04	0	0.28	0	-0.15/-0.13
8	0	0.01	0	-0.42	0	0.11	0	0.05/0.06
10	0	-0.21	0	0.05	0	-1.43	0	-1.53/-1.92

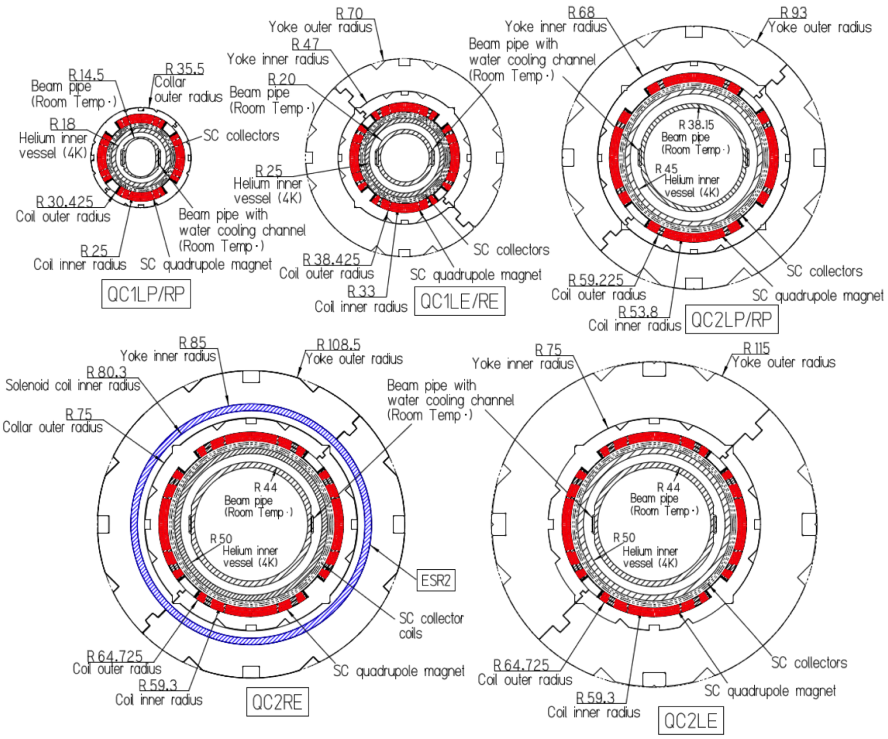

Figure 5.5: Quadrupole magnet cross sections.

and B_1 correctors are designed to be able to shift the magnet axis in the range of 0.5 mm to 1.0 mm, in the horizontal and vertical direction, respectively. The A_2 corrector can rotate the mid-plane of the quadrupole field phase from 12 mrad to 15 mrad in the amount of angle. The B_4 corrector magnets increase the dynamic transverse aperture. The corrector magnet production for QCS-L commenced first using preliminary specifications provided before the right-side requirements were set. Later optics studies found that sextupole A_3 and B_3 correctors are needed in order to cancel the error fields of the quadrupole magnets induced by magnet assembly errors. The required integral sextupole field strengths are equivalent to 1×10^{-3} of the quadrupole fields. Installation of sextupole correctors was decided from the magnetic field measurement results of QC1P/1E proto-type magnets [7].

The majority of the corrector coils are located inside a main quadrupole coil; however, with insufficient space inside the QC1LP/RP quadrupole magnet bores, their B_4 correctors are wound on bobbins places just outside the main coil (along with the A_3 and B_4 correctors for QC1RP). Because these QC1LP/RP quadrupoles have insufficient space for magnetic flux return yokes between their coils and the nearby HER beam, there is significant external field leakage that must be dealt with so as not to adversely impact the HER optics. Requirements for these additional external field

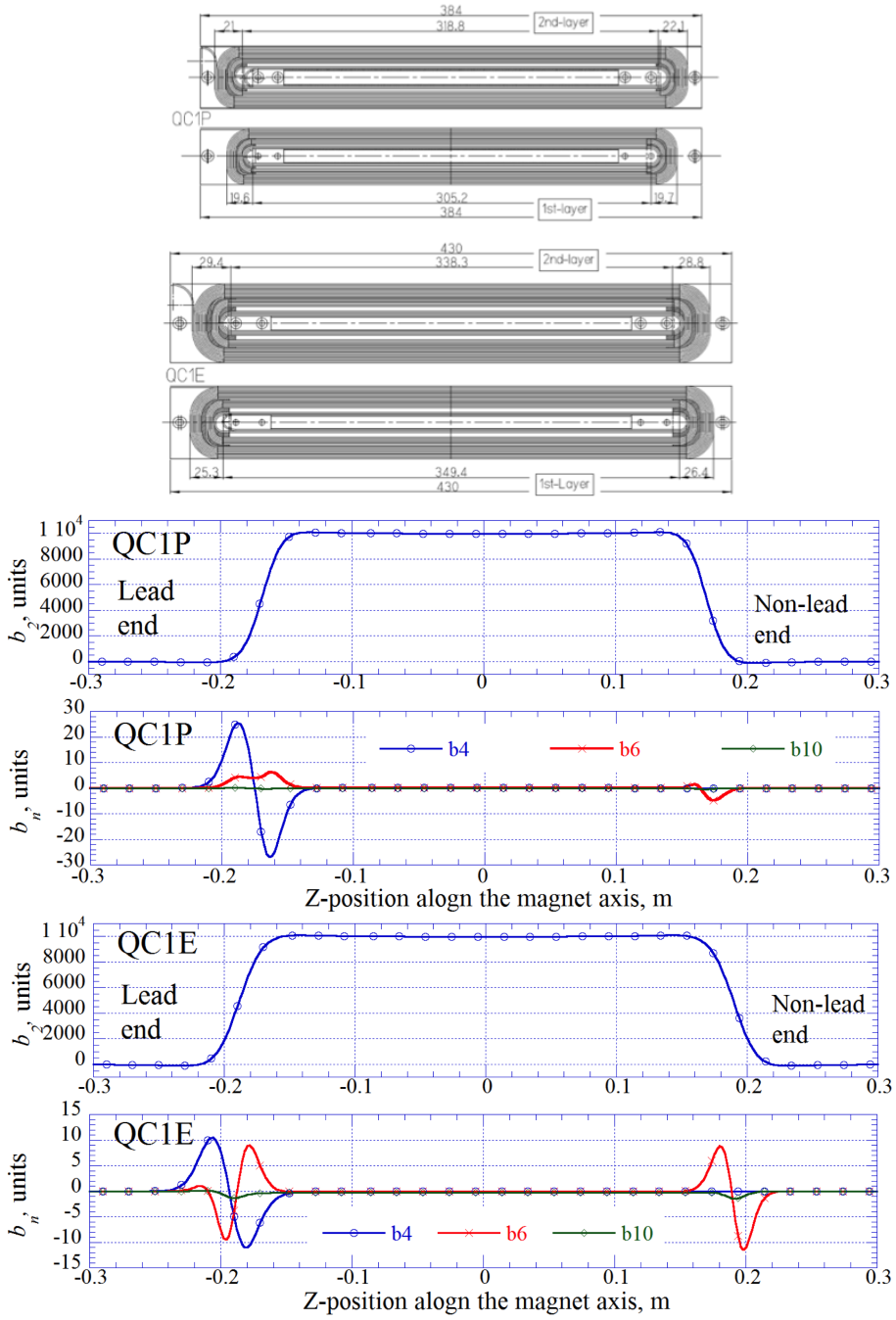

Figure 5.6: Two layer coil geometries and multipole field profiles along the magnet axes of QC1P and QC1E. Z-position=0 is the magnet center, and the reference radii are 10 mm and 15 mm for QC1P and QC1E, respectively.

Table 5.7: Corrector integral field requirements. The right-side b_3 magnets are places between main magnets. The leakage field cancel magnets for the HER are not included in this table.

Magnet	R_r mm	A_1 T m	B_1 T m	A_2 T	A_3 T/m	B_3 T/m	B_4 T/m^2
QC1RP	10	0.016	0.016	0.64	7.6	17.2	60
QC2RP	30	0.03	0.03	0.31	1.36	@R_r=30	-
QC1RE	15	0.027	0.046	0.75	7	27	-
QC2RE	35	0.015	0.015	0.37	1.5	@R_r=15	-
QC1LP	10	0.016	0.016	0.64	-	-	60
QC2LP	30	0.03	0.03	0.31	-	-	60
QC1LE	15	0.027	0.046	0.75	-	-	60
QC2LE	35	0.015	0.015	0.37	-	-	60

cancel coils for the HER are discussed in Chapter 1.

Both the corrector and cancel coils are attached to support bobbins via the Direct Wind technique using 0.35 mm diameter, single-strand superconducting round wire from Furukawa with a 1:1 Cu:NbTi ratio and critical current at 4.2K greater than 130 amps in a 5 T background field [5]. The wire is Kapton® overwrap insulated and adhesive coated to be compatible for use with BNL Direct Wind ultrasonic bonding technology.

5.2.4 Compensation solenoid design

Figure 5.9 shows the solenoid field profile (red line with dots) only by the Belle-II solenoid and the combined field profile (black line) with ESL, ESR1, ESR2 and ESR3 with the locations of the quadrupole magnets. As shown in Fig. 5.9, the Belle-II solenoid generates the solenoid field of 1.5 T at the center of the detector, and the field is mainly cancelled by the reverse solenoid fields by ESL and ESR1 in the areas of QC1LP and QC1RP. In order to produce the combined solenoid field profiles required by beam optics, ESL and ESR1 are divided into 12 and 15 small solenoids as shown in Fig. 5.10, and they produce the integral fields of 2.31 T m and 3.69 T m, respectively. These integral fields correspond to the integrated Belle-II solenoid fields from the IP. The maximum fields in the ESL and ESR1 coils with the Belle-II fields are 3.4 T and 3.2 T, respectively.

Since the QC1E magnets and the QC2P magnets have the Permendur yokes and

Table 5.8: Design Parameters of Compensation Solenoids.

	ESL	ESR	ESR2/3
Magnet			
Integral field, T m	2.31	3.69	0.17
Design current, A	390	450	151
Inductance, H	2.5	8.0	0.14
Maximum field, T	3.4	3.2	0.48
Magnet length, mm	905	1575	720
No. of component coils	12	15	1
Total turns	4610.1	6237.1	1356
I_d /$I_{c,\ \%}$	52	51	11
Superconducting cable	NbTi		
I_c at 4T and 4.22 K, A	1814		
Cu/NbTi ratio	1.7		
Cable size, mm	0.932×1.384		

the counter beam lines are covered by the magnetic shields, the combined fields on the beam lines are designed to be less than 0.01 T. The residual solenoid fields on the beam lines are negligible on the beam lines. Between QC2RP and QC2RE, the Belle-II fringe field is in the range of 0.6 T because of no magnetic shields. This fringe field is cancelled by the ESR2 on HER or the ESR3 solenoid on LER in the area of QC2RE. The solenoid parameters are summarized in Table 5.8.

5.2.5 Cryostat

Cryostat system design

Two cryostats are designed to be installed on each side of IP as shown by Fig. 5.2, the QCS-L cryostat for the left side and the QCS-R cryostat for the right side. The cross sections of the QCS-R cryostat are shown in Fig. 5.11 [8]. The QCS-L cryostat has the same configuration as QCS-R. The cryostat consists of a magnet cryostat, a service cryostat, a cryogenic tube and a support table. The magnet cryostats are supported in a cantilever way inside the Belle-II detector by the support table, as shown in Figs. 5.2 and 5.11. The cryostat parameters are listed in Table 5.9.

As shown in Fig. 5.11, the superconducting magnets are assembled in the two helium vessel (front vessel in IP side, and rear vessel in non-IP side). At the service

cryostat, the cryogenic transfer tubes from the cold box are connected to the cryostat. The current leads are mounted in the service cryostat. Since each magnet is connected to the individual power supply, the QCS-L and QCS-R service cryostats have 25 pairs plus 1 leads and 29 pairs plus 1 current leads, respectively. The ESR2 and ESR3 have the same magnet parameters, and then these solenoid magnets are connected in series. The current leads for the QC1/QC2 magnets and the ESL and ESR1 solenoids are conventional types which are cooled with vaporized helium gas. The current leads for the corrector magnets and the ESR2/3 solenoids are compact assembled unit where 8 leads are embedded [9]. The leads have the HTS superconducting tapes in the low temperature region below 80 K to reduce the heat load by 0.24 W/unit due to joule heating, and the leads are cooled with the evaporated He gas. The additional 1 lead is for tuning the solenoid field profiles along the axes of ESL and ESR1. In the front vessel, the radiation shields of tungsten alloy of which density is 18 g/cm^3 are installed in order to protect the Belle-II components. The total weights of the radiation shield are 231 kg and 1271 kg for QCS-L and QCS-R, respectively.

Concerning for the 80K thermal shield in the magnet cryostats, SS304 as the material was used for reducing an eddy current by magnet quench. The eddy currents generate electro-magnetic force (EMF) and deformation of the shield plate. Because of a low thermal conductivity of SS304, the temperature profile of the plate was calculated, and the temperature difference in the plate was confirmed to be within 5 degree. In the service cryostat, aluminum alloy was used because of high thermal conductance and the very weak background magnetic field.

The material of the support table was SS400 because the tables had the function as the magnetic shield against the fringe field from the Belle-II solenoid for the conventional magnets which were assembled inside of the table.

Mechanical design of the cryostat

The helium vessels are supported by a suspension system of eight titanium alloy (Ti-6Al-4V) rods. In Fig. 5.12, the system for the front vessel of the QCS-R cryostat is shown. The lengths of the rods are 75.5 mm and 108 mm in the front and back sides, respectively. The rods are designed to have a tilt angle so that the center between the supporting points of the rods on the helium vessel does not change when the vessel is cooled down to 4K. The angles of the front and back rods at room temperature are 20.16 degree and 20.14 degree, respectively, and after cool-down to 4 K, they are changed to 18.83 degree and 19.72 degree, respectively. With thermal contraction during cool-down, the quadrupole magnet centers change as shown in Fig. 5.4. The QC1RP center changes 2.35 mm and 0.12 mm in the axial and horizontal directions,

respectively. The magnets and components at 300 K are designed so that the magnet centers at 4 K are positioned on the beam lines.

As the result, the axial repulsive EMFs act on the solenoids. The calculated values are summarized in Table 5.10. The EMFs on the ESL and ESR1 are 52.6 kN and 35.7 kN, respectively. By these forces, the front helium vessels where the solenoids are placed are pushed out from IP. In case that the ESL and ESR1 solenoids are not excited like a magnet quench, the magnetic components in the vessels are drawn into IP, and the forces are calculated to be 57.3 kN and 23.5 kN, respectively. The rods are designed to withstand the forces and the weight of the helium vessel. The cross section areas of the rods for QCS-L/R are 182.3 mm^2 and 81 mm^2, and the maximum stress in the rods is 174 MPa and 205 MPa, respectively. The stress is sufficiently smaller than the yield strength of the titanium alloy at room temperature (825 MPa).

Thermal design of the cryostat

The thermal design of the magnet cryostat is based on the condition that the superconducting magnets are cooled with single phase liquid helium (LHe) for the stable magnet excitations during the SuperKEKB beam operation. Each cryostat is cooled with the individual helium refrigerator of which the cooling power is 250 W at 4.4 K. The cryogenic system can supply subcooled LHe of 20 g/s to the cryostat. LHe at the inlet of the cryostat is in a subcooled condition at 0.161 MPa and 4.4 K. The allowable thermal load to the helium vessels is 40 W for the helium to be subcooled. The thermal loads for two cryostats were calculated and the results are summarized in Table 5.11. In the magnet cryostats of QCS-L and QCS-R, the loads are 16.3 W and 15.9 W, respectively. Both loads are below 40 W and all magnets can be cooled by subcooled LHe.

In this thermal design, while the outer surfaces of the helium vessels have the thermal radiation shields cooled by liquid nitrogen, the surfaces of the bores for the beam pipes do not have the thermal shield because of the limited space between the bores and the pipes. In Fig. 5.13, the horizontal cross section of the front part of the QCS-R cryostat is shown. The helium vessel has two bores at 4 K for the beam pipes at 300 K, and the corrector magnets are directly attached to the outer surfaces of the bores. The QC1RP magnet is assembled outside of the corrector magnets. The right figure shows the QC1RP cross section in detail. In the design, the minimum distance between the bore and the beam pipe is only 3.5 mm. In order to reduce the heat load by thermal radiation, the beam pipes are wrapped with 5 layers of a superinsulation sheet, and the bore surface of SS316L is mirror-processed and coated with Al by a vapor deposition. The emissivity coefficient of this bore surface is evaluated to be smaller

than 0.02, and the heat load by the thermal radiation is reduced by 50 %, compared to the surface of SS316L as the bore material.

The QCS-L and QCS-R service cryostats have 16 and 17 ports for installing the current leads, respectively. The pipes of the ports are connected between the vacuum vessel and the cooling pipe, and the thermal loads through the pipes of QCS-L and QCS-R are 11.5 W and 12.5 W, respectively. After cooling the magnets, LHe of about 1 g/s is used for cooling the current leads, and then the total thermal loads of the QCS-L/R cryostats are 40.5 W + 1.00 g/s and 40.7 W + 1.03 g/s, respectively.

5.2.6 Cryogenics

The magnet-cryostat at each side of IP is cooled with the individual cooling system. The cooling system consists of a helium refrigerator, a helium compressor, a liquid helium subcooler, two helium gas tanks and a liquid nitrogen storage tank. The helium refrigerator and the liquid helium subcooler are installed in the 4^{th} basement of the Tsukuba experimental building as shown in Fig. 5.14. The subcooler and the magnet-cryostat are connected with the multi-channel cryogenic transfer tube. The pressurized helium gas at 5K supplied by the refrigerator is changed in the subcooled liquid helium at 4.44 K and 0.161 MPa with the heat exchanger. The system can supply the subcooled liquid helium of 20 g/s for one cryostat. The subcooled liquid helium can cool the heat load of 40 W under the condition of the liquid phase. The evaluated heat load to the helium vessels in the cryostat is 23.9 W. In the thermal design of the cryostat, the margin of the heat load is 15.5 W. The measured cooling power of the helium refrigerator is 160W + 28.4 L/h. The total heat load of the system is calculated to be 85.2 W + 28.4 L/h. The refrigerator has the margin of 74.8 W. The heat loads of one system are summarized in Table 5.12.

5.3 Beam pipe and vacuum system

5.3.1 IP chamber

The inner profile of the IP chamber is determined by taking account of following conditions.

- The middle part is a straight pipe parallel to the magnetic field of Belle II with a diameter of 20 mm.
- Make no cavity inside the IP chamber so that HOM created by a crotch may propagate away.

Table 5.9: Cryostat parameters.

	QCS-L	QCS-R
Magnet cryostat		
Vac. vessel length (mm)	2724	3287
Vac. vessel max. diameter (mm)	ϕ1100	ϕ638
Vac. vessel mass (kg)	1570	1472
4 K Cold Mass		
Front magnets and others (kg)	949	805
Tungsten radiation shield (kg)	231	1271
Rear magnets and others (kg)	342	1063
80 K thermal radiation shield (kg)	45	36
Service cryostat		
Vac. vessel length (mm)	2757	2757
Vac. vessel height (mm)	917	917
Vac. vessel wide (mm)	900	863
Vac. vessel mass (kg)	2523	2501
80 K thermal rad. shield, kg	79	77
He gas-cooled current leads		
Conventional leads	10 pairs+1	10 pairs
Compact 8 terminal leads	5 units	7 units
Control valves	2	2
Support table		
Length, mm	3810	3810
Mass, kg	6279	6061
Total cryo. system length (mm)	6533	7087
Total cryo. system mass (kg)	12550	15000

Table 5.10: Electro-Magnetic forces on ESL, ESRs and iron components.

	Excitation	EMF on solenoids, N	EMF on iron, N	Total, N
QCS-R	ON	3.58×10^4	-0.60×10^4	2.98×10^4
	OFF	0	-2.37×10^4	-2.37×10^4
QCS-L	ON	-4.69×10^4	0.42×10^4	-4.27×10^4
	OFF	0	8.04×10^4	8.04×10^4

Table 5.11: Design heat load of cryostats at 4 K

	QCS-L	QCS-R
Magnet cryostats		
Support rod, W	9.7	5.8
Thermal radiation, W	6.6	10.1
Sub-total, W	16.3	15.9
Service cryostat		
Thermal radiation, W	1.9	2.1
Current lead pipe, W	11.5	12.5
Instrument wire, W	3.8	3.4
He gas for C. L., g/s	1.00	1.03
Sub-total	23.2 W + 1.00 g/s	24.0 W + 1.03 g/s
Total	40.5 W + 1.00 g/s	40.7 W + 1.03 g/s

Table 5.12: Estimated heat load and the required amount of liquid helium for the QCSL cryogenic system.

Cryostat	(including the service cryostat)	40.5 W	
Current Leads	QC1P, QC1E, QC2P, QC2E, ESL	-	24.4 L/h
	20 corrector magnets	-	4.0 L/h
Transfer Tube	˜13 m length + 1 connection box	16 W	
Total		56.4 W	28.4 L/h

- Allow no direct hit of SR on the middle pipe from the final bend, and stop other SR as possible as one can.

Figure 5.15 shows a plane view of the inner profile.

The design of the middle straight pipe of the IP chamber is shown in Fig. 5.16. The 'window' through which elementary particles from IP appears of is double beryllium tubes. The 'window' is open to an azimuthal angle from 17 degree (forward) to 150 degree (backward). The thickness of the inner beryllium tube is 0.6 mm and the inner diameter is 20 mm. The outer tube has a 1 mm gap with respect to the inner tube and has a thickness of 0.4 mm. They are brazed to titanium manifolds. The gap is used to cool the inner pipe with paraffin. Paraffin is provided through the titanium manifolds. Mechanical structure of the titanium manifolds is able to absorb the difference of expansion between two beryllium tubes. This straight pipe is sputter-coated with 10˜20 μm gold to stop scattered photons below 10 keV. The uniformity of the coating is tested with a model tube. It was within 5% fluctuation for a beryllium part.

Titanium manifolds are welded to tantalum branch chambers via Ti-Ta transition. The tantalum chambers are sputter-coated with 10 μm copper to reduce the ohmic loss of wall current. The beam pipe in the branch chamber for incoming beam has a slope towards the interaction point to reduce direct irradiation of SR through the pipe from the final bend. Since the SR from the last bend illuminates only outside wall (lower side in Fig. 5.15) of the beam duct, the direct SR passes through the central tube without hitting its wall. The minimum diameter of the beam pipe for an in-coming beam is 10 mm. At this narrowest aperture, a $30\sigma_{\mathrm{x}}$ radius of the beam is 2˜3 mm. Therefore it is sufficiently large for the beam. The whole view of the IP chamber is shown in Fig. 5.17 with some fabrication information. The IP chamber has a mechanically delicate central pipe and heavy wings. Though it is confirmed by mechanical analysis by S. Koike (MEC) that the IP chamber is self-supporting, handling must be done with care.

To avoid the hitting of scattered light on the beryllium surface, the inside of the pipe for an in-coming beam has ridges. The beryllium surface is hidden in a space defined by the illuminated slope of ridges. The effectiveness of the ridge structure depends on the amount of photons which may reach the beryllium surface due to tip-scattering on top of the ridge. T. Ishibashi and K. Sonnard (Cornell University) performed very clear experiment at Chess G2 beam line (Cornell University) on this issue. A gold coated ridge of tantalum is illuminated by the 9 keV photon beam. One side of the ridge is vertical. The other side has a slope of 18.4 (Fig. 5.18 (a)). The top of the ridge has a fillet of 0.5 R. The vertical beam size is about 0.14 mm. The boundary of the beam is not clear-cut due to scattering on air. The sample is set so that half of the beam hit

the ridge. As seen by the vertical beam size, the beam hit only the fillet of the ridge. The ratio of photons scattered off from the primary beam was measured. The set up geometry is shown in Fig. 5.18 (b). The result is shown in Fig. 5.18 (c). From this result, one can see that the number of photons scattered into the hidden space by the slope of the ridge is negligible. This experiment was performed using a monochromatic light. However it gives clear suggestion on an amount of tip-scattered photon.

The pipe for outgoing beam has the same diameter as the middle straight pipe to allow for created HOM to escape. The structural loss factor of the IP chamber is calculated by K. Shibata with GdfidL for each version of the design. At present we don't have estimation for the last design. We refer here the estimation just before the last as 1.67 x 10^{10} V/C (for a bunch length of 5 mm), 1.10 x 10^{10} V/C (for a bunch length of 6 mm). The power loss of the beam is 458 W for HER, and 574 W for LER. The contribution of the ridge in the impedance is about 20˜60 %.

5.3.2 Ta beam pipe in the cryostat

To place final focus magnets as close as to the interaction point, the inner bore of QC1 is minimized by using a warm inner bore of the cryostat as a beam pipe. The thickness of this beam pipe is 4 mm. The inner diameter changes in four steps as shown in Table 5.2. Its vertical dimension is elongated in QC1RP and QC1LP. The central axis of the electron beam pipe has a horizontal offset of 0.7 mm between QC1 and a remaining front part. It is made of Ta according to the requirement by the detector group. Cooling water is necessary to absorb heats due to the direct SR from the last bending magnet and the ohmic loss on a wall. Inside of the beam pipe is coated with 10 micron Cu to reduce the wall loss. Beam position monitor is installed on this pipe. A typical image of this pipe is shown in Fig. 5.19. Since this beam pipe is surrounded with He-temperature surfaces, a care is necessary not to freeze cooling water. As the outside of these beam pipes is limited, water channel must be designed closely along the body. At some locations water passes a welded seam whose other side is a vacuum. This kind of structure is avoided in a standard design. However, because Ta is chemically stable, we judged that no corrosion will develop. As an R&D we made a short Ta pipe, which has a cooling channel in the wall and a welded seam between water and vacuum. After a test with tap water over months, no water leakage was observed. At the same time it is found Ta has a very low thermal outgassing rate (H. Hisamatsu, see 3-4).

5.3.3 Other beam pipes and Pressure estimation

Other beam pipes within the first gate valves from IP are made of copper. Their standard inner diameter is 80 mm. The duct for positron bending magnet has a groove on top and bottom to reduce the electron cloud density. To fabricate this groove, straight beam pipe is adopted for a bending magnet, which reduces the horizontal aperture. All positron beam pipes outside cryostat are TiN coated also to reduce the electron cloud density. The main pump in this region is non-evaporable getter (NEG). NEG strip is installed as a distributed pump along a bending chamber. Between magnets high-capacity NEG modules are installed at pump ports. The arrangement of vacuum pumps is shown in Fig. 5.20. From IP to the end of the cryostat, no space for vacuum pump is available. The average pressure around IP will be of the order of 10^{-6} Pa even after sufficient scrubbing with SR (when photo-desorption coefficient of the QCS beam pipe is ~ 10^{-6} molecules/photon). Detailed calculation of the pressure profile around IP is planned.

5.3.4 Some experimental vacuum data

Special material and coating are used in vacuum components of this region. To compare with standard material with respect to thermal desorption and photon-desorption property, some measurements are performed. Though they not always directly applicable to the final design, those data are useful from a general viewpoint and are reported here.

Photon desorption coefficient of Ta, Cu, Au-coat on Ta (Y. Tanimoto and T. Nogami)

Photo-desorption coefficient was measured at the beam line BL21 of Photon Factory (PF). The source of synchrotron radiation is a bending magnet and the critical energy of SR is 4 keV. A sample was exposed to 5 mm x 5 mm photon beam at normal incidence. The value of each desorption coefficient is similar up to a photon dose of 10^{21}. Then the decrease of the desorption coefficients of Ta and Au become slower than Cu. And Au shows much slower decrease. At present we have no explanation on the reason why the decrease of the desorption coefficient of inactive material becomes slow at high photon dose. These data are shown in Fig. 5.21 (a)-(c).

Thermal outgassing rate of Ta pipe (H. Hisamatsu)

A test pipe is 478 mm long. A 346 mm tube with ID 21 mm is connected to a 34 mm long ID 26 mm tube with a taper. It was cleaned with HNO_3 + HF + Water. Then it was heated in a vacuum furnace with a cryo-pump at 1100-1150 °C. The outgassing rate is shown in Fig. 5.21 (d), The outgassing rate is lower than standard titanium and copper.

5.4 Installation scenario

We have vacuum connections between IP chamber and cryostat beam pipe. The access by human hands to these connections at their final location is impossible in the forward part, and is difficult in the backward part. How to connect these flanges is combined with how to install the vertex detector (VXD). At present two options are considered.

Baseline scenario

First VXD and QCSR are connected outside the detector. Then QCSR moves forward pushing VXD. After VXD is mechanically detached from QCSR and fixed on CDC, QCSL moves forward. Then remaining connection is performed by hand. The last step is now becoming more difficult with an advance of detailed detector design and cryostat design. This scenario assumes the Belle II detector is in the roll-in position. When the replacement of the BPM-bellows unit is necessary, VXD must be pulled out. Fig. 5.22 illustrates the whole process of this scenario.

Alternative installation method (AIM)

This method makes use of a remote vacuum connection system (RVC) in front of the cryostat. The RVC system was proposed by K. Gadow and C. Niebuhr (both DESY). The prototype of the RVC was tested and succeeded in performing vacuum connection. A 3D-picture of the prototype and a mock-up are shown in Fig. 5.23. In this case VXD is installed by hand using some sliding supports. A concrete design of this support system is being developed and tested at MPI by C. Kiesling and B. Müller. The Major concern is that the use of RVC in the forward inaccessible region. A disassembling method in case the RVC stacks must be established.

5.5 Radiation shield

New concrete shields are added to an existing gate shield.

1) On top of the gate shield 45 cm concrete is added.
2) Front of the gate shield is filled with concrete leaving a necessary aperture for accelerator components..
3) The gap between the detector and Accelerator floor is filled with concrete.
4) The gap between the ceiling of accelerator tunnel and the gate shield is filled with 80 cm concrete.
5) The shield wall of the experimental hall is extended towards IP.
These additional concrete shields are depicted in Fig. 5.24 except 3). By these concrete shields, the radiation level of the experimental hall will be 1˜10 μSv/h for design parameters. A training as a radiation worker is necessary to access the hall. To reduce further, local shield around radiation sources will be added. Especially beam pipes where the beam loss due to the radiative Bhabha process occurs must be shielded to reduce air activation. It is suggested that shields to cover an opening for cable trays connecting the experimental hall and the accelerator tunnel are effective to reduce the radiation level of the hall. (T. Sanami)

5.6 The design for Phase 1 commissioning

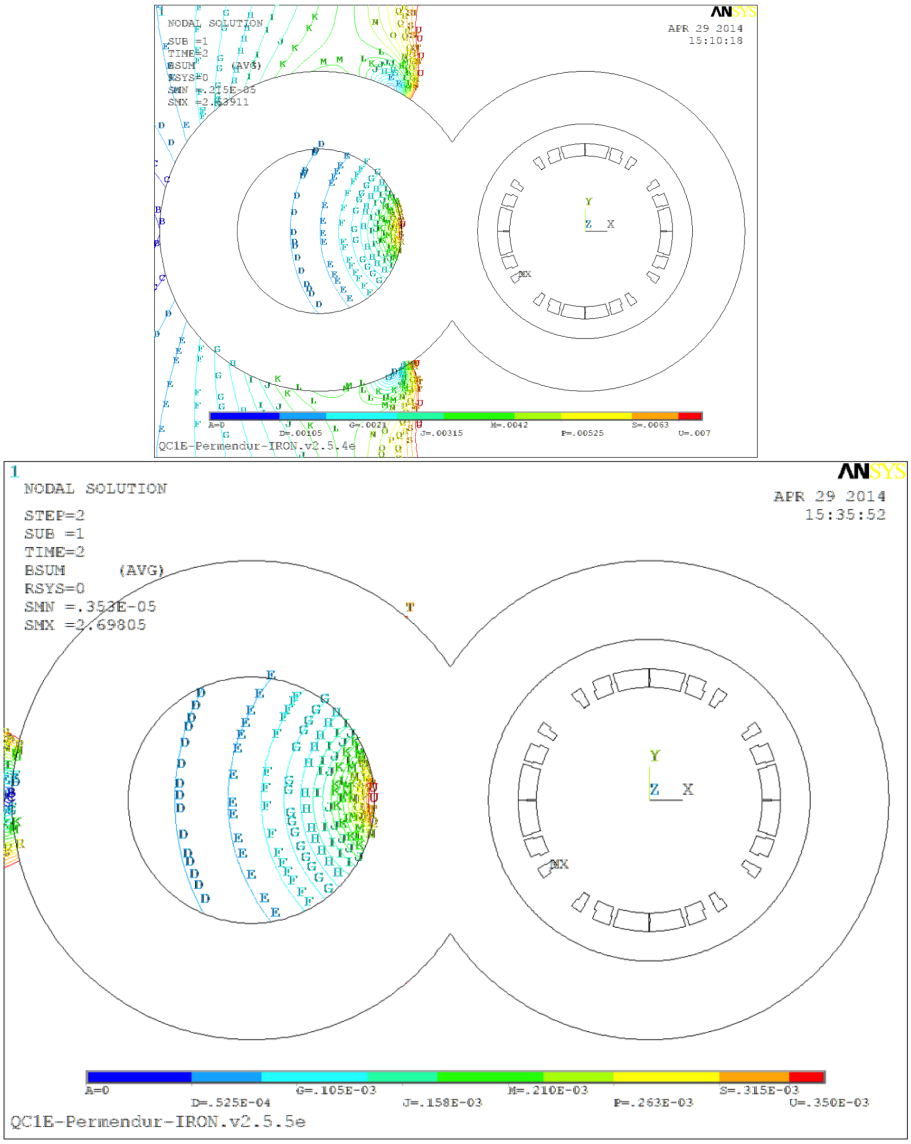

Figure 5.7: Contour plots of the magnetic field in the positron beam line laying side-by-side with QC1LE. QC1LE magnet current is 1577 A as 4s operation. In the upper plot, the materials of the QC1LE yoke and the magnetic shield of the position beam line are iron, and in the lower plot, they are Permendur.

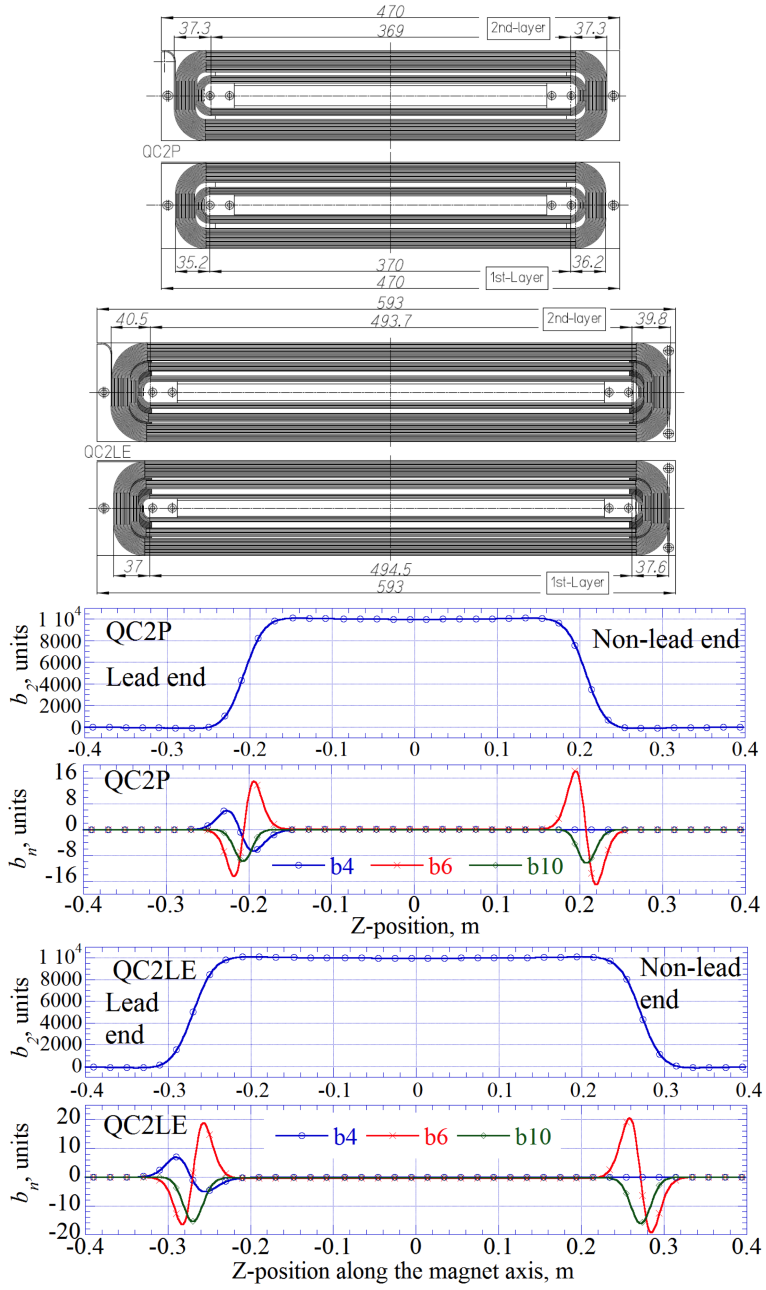

Figure 5.8: Two layer coil geometries and multipole field profiles along the magnet axes of QC2P and QC2LE. Z-position=0 is the magnet center, and the reference radii are 30 mm and 35 mm for QC2P and QC2LE, respectively.

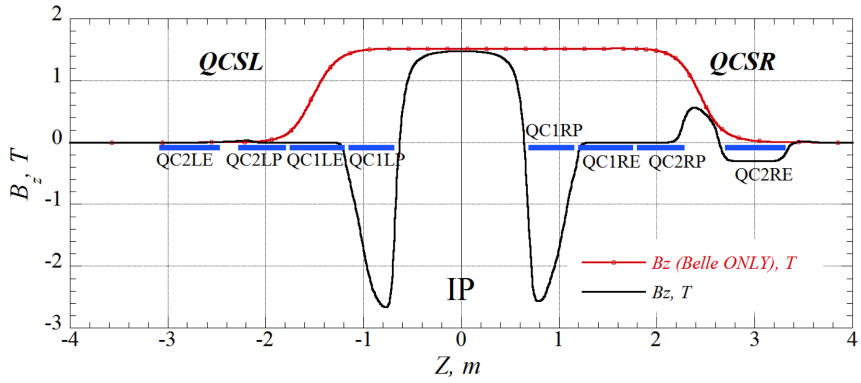

Figure 5.9: Solenoid field profiles along the beam lines.

(a)

(b)

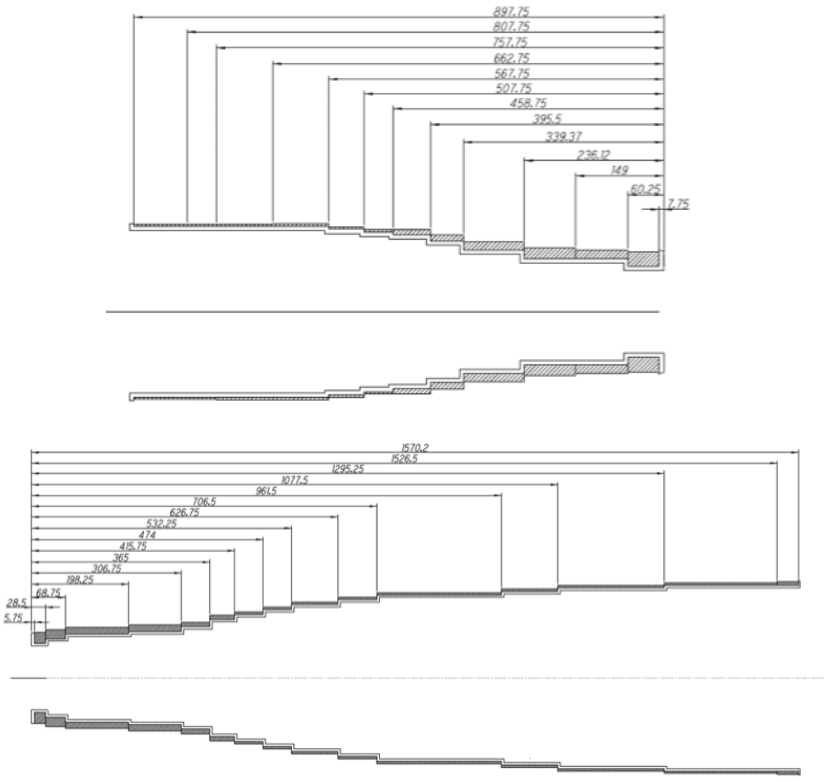

Figure 5.10: Compensation solenoids. The drawings of (a) and (b) show the ESL and the ESR1 solenoid magnets, respectively.

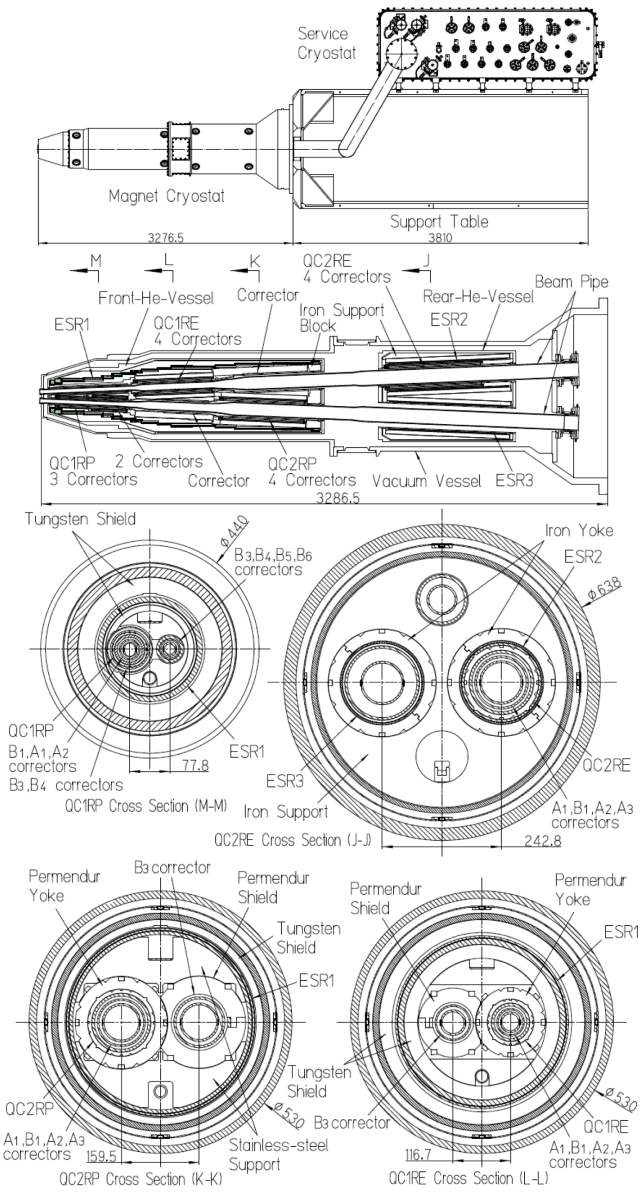

Figure 5.11: Overall view of QCS-R cryostat and the cross section of the magnet cryostat. The top figure is the whole cryostat viewed from the top. The middle figure is the horizontal cross section of the magnet cryostat, and the bottom figures are the vertical cross sections of the magnet cryostat at the individual quadrupole magnet center.

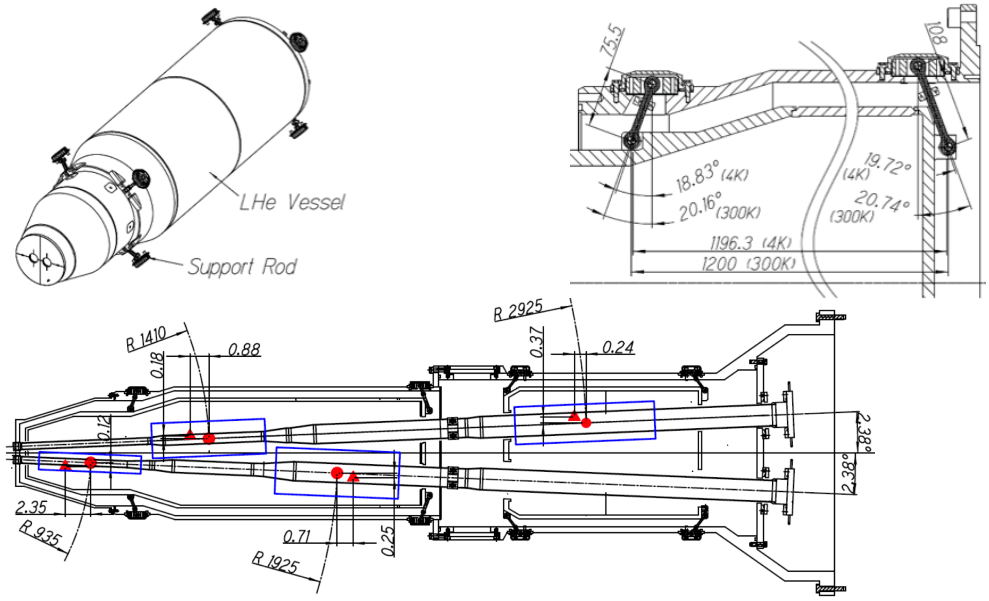

Figure 5.12: Support rods of the front helium vessel of the QCS-R magnet cryostat (top left), the rod design (top right) and the magnet center changes of four quadrupole magnets by cool-down (bottom). The quadrupole magnet centers at 300 K and 4 K are shown with symbols of triangle and circle, respectively. The position changes are shown in mm.

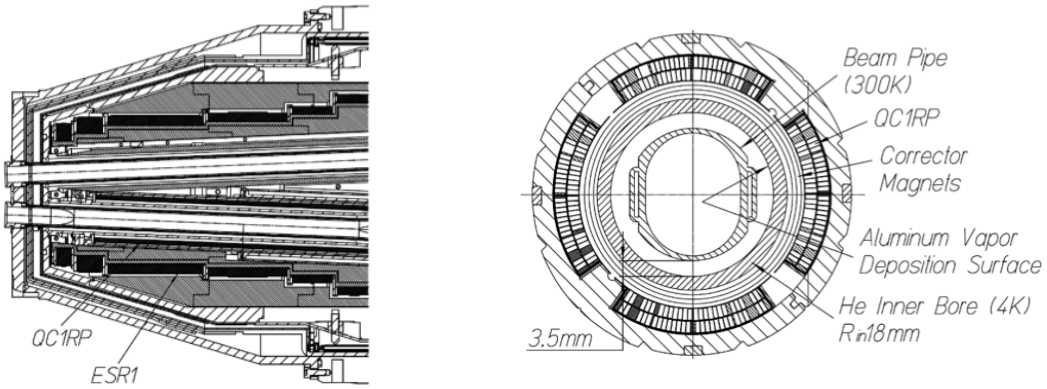

Figure 5.13: Cross section of the front part of the QCS-R magnet cryostat. The left figure shows the horizontal cross section of the QCS-R cryostat at the QC1RP magnet. The right figure is the QC1RP cross section.

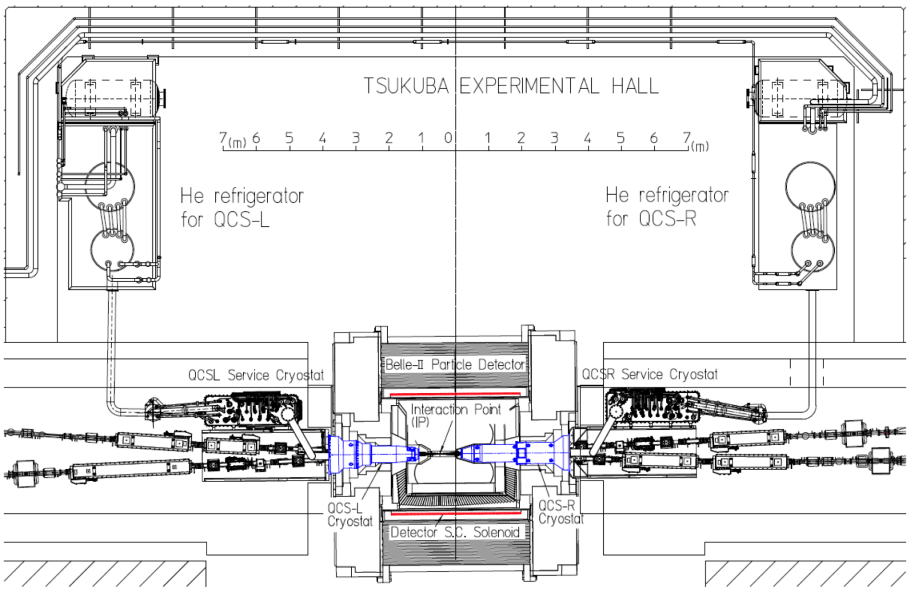

Figure 5.14: Cryogenic systems for the final focus superconducting magnet system.

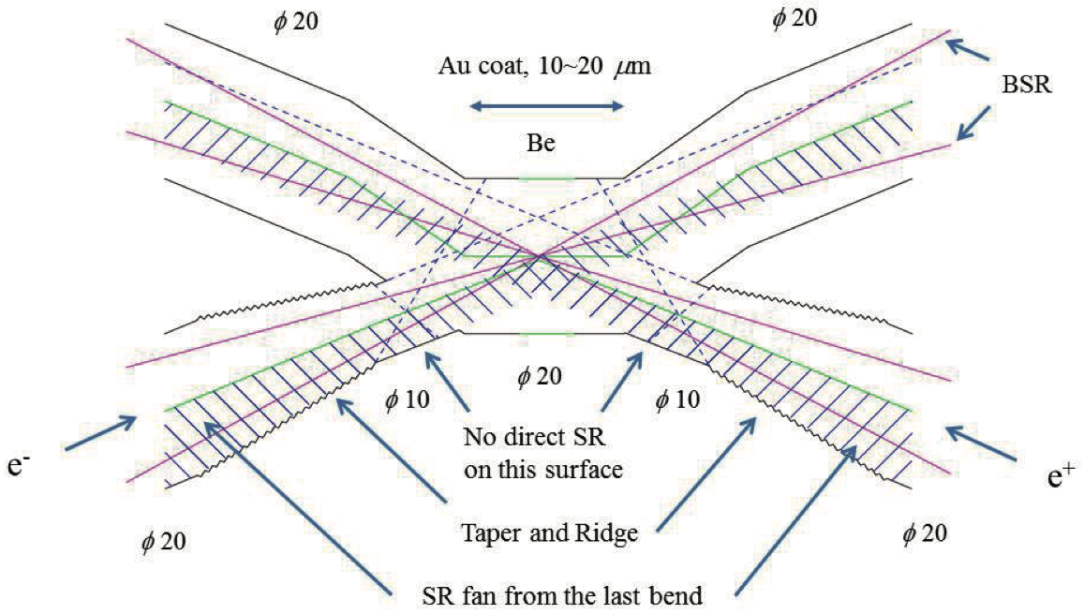

Figure 5.15: Inner profile of the IP chamber. Vertical scale is expanded ten times. BSR (beam stay clear) corresponds to about $30\sigma_x$ radius.

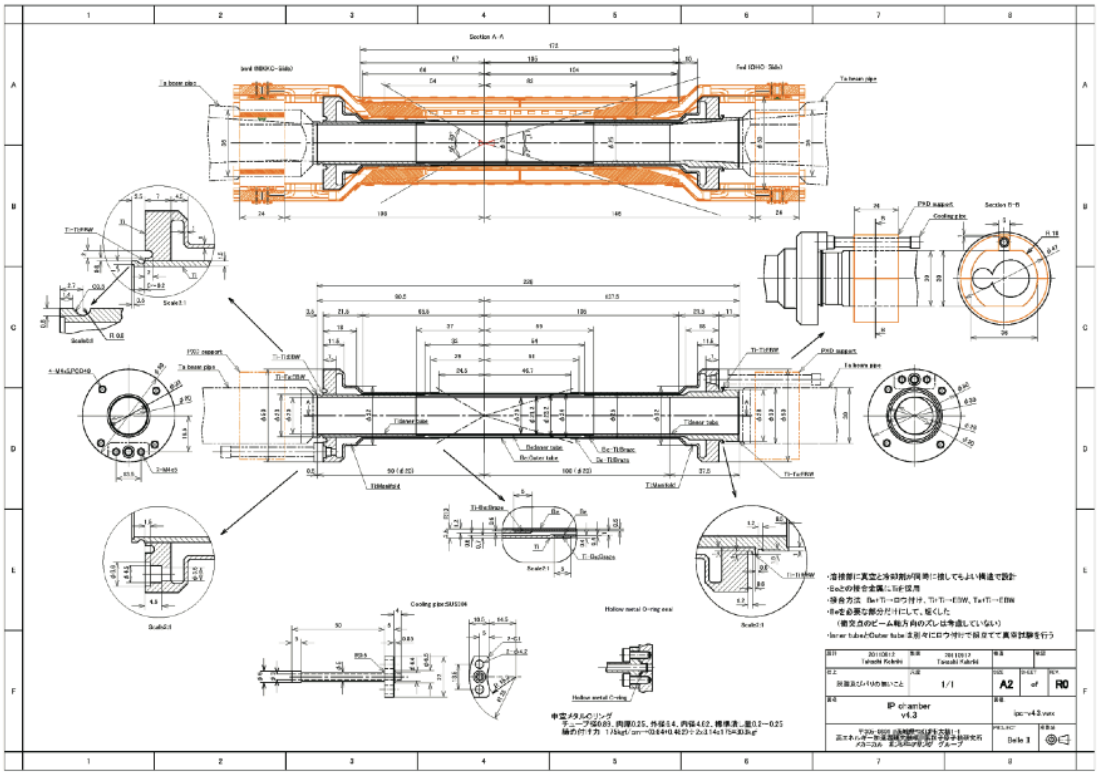

Figure 5.16: The middle straight pipe of the IP chamber designed by T. Kohriki (IPNS).

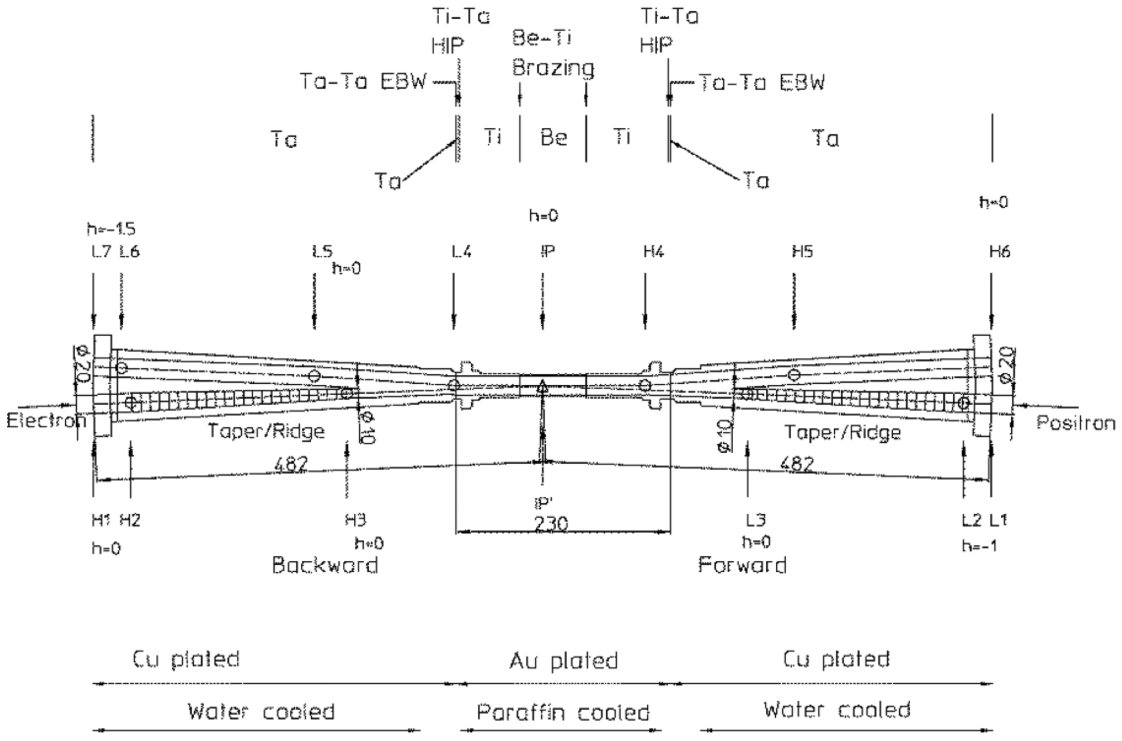

Figure 5.17: Whole view of the IP chamber.

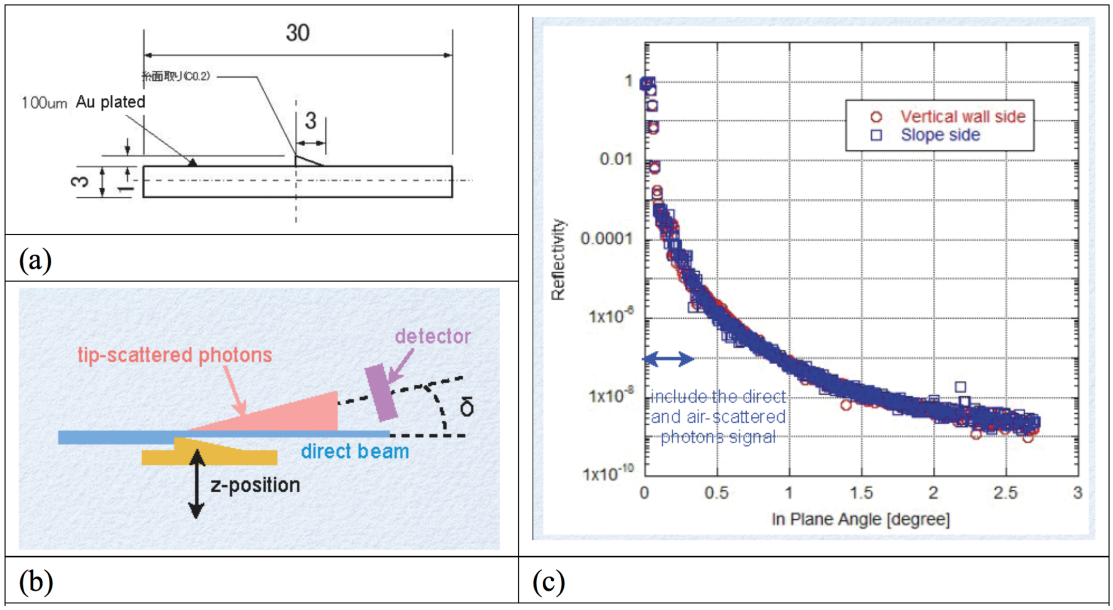

Figure 5.18: Measurement of the tip-scattering of photon. (a) Sample dimension. (b) Experimental set-up. (c) The ratio of scattered photon with respect to the primary beam. The horizontal axis of this graph is 'δ' in the picture of (b).

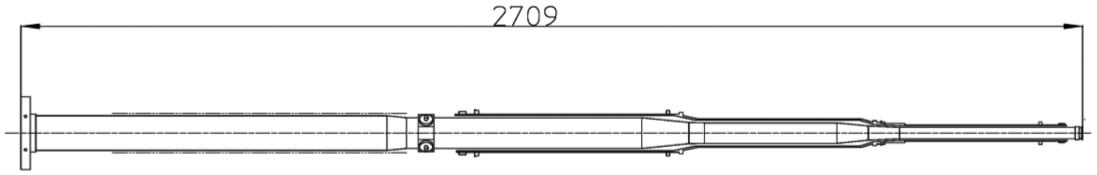

Figure 5.19: Ta beam pipe for QCSL positron beam line.

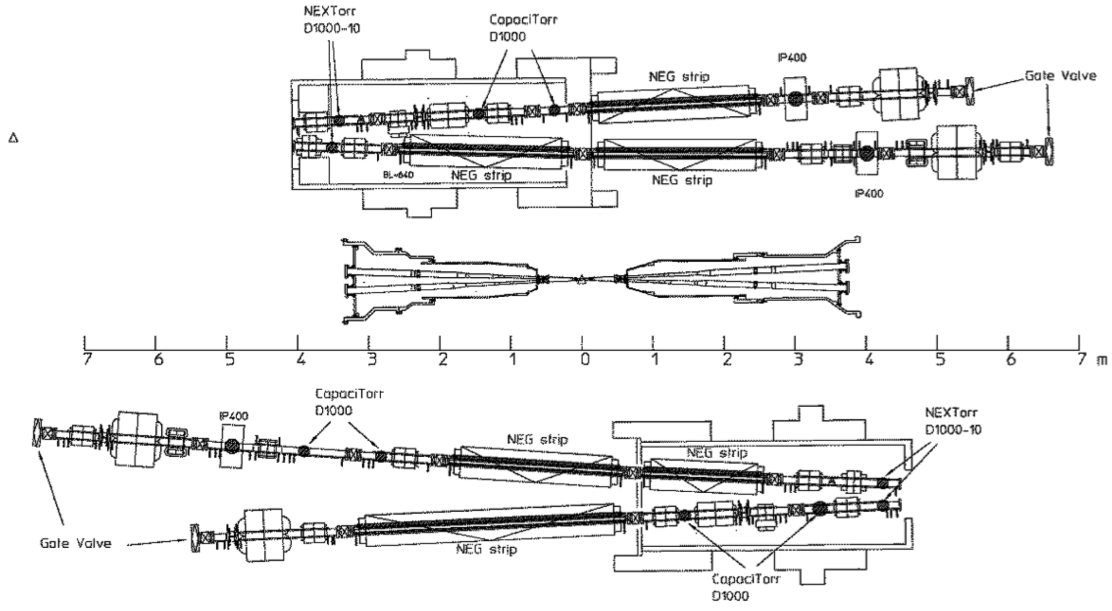

Figure 5.20: Arrangement of vacuum pumps in the interaction region.

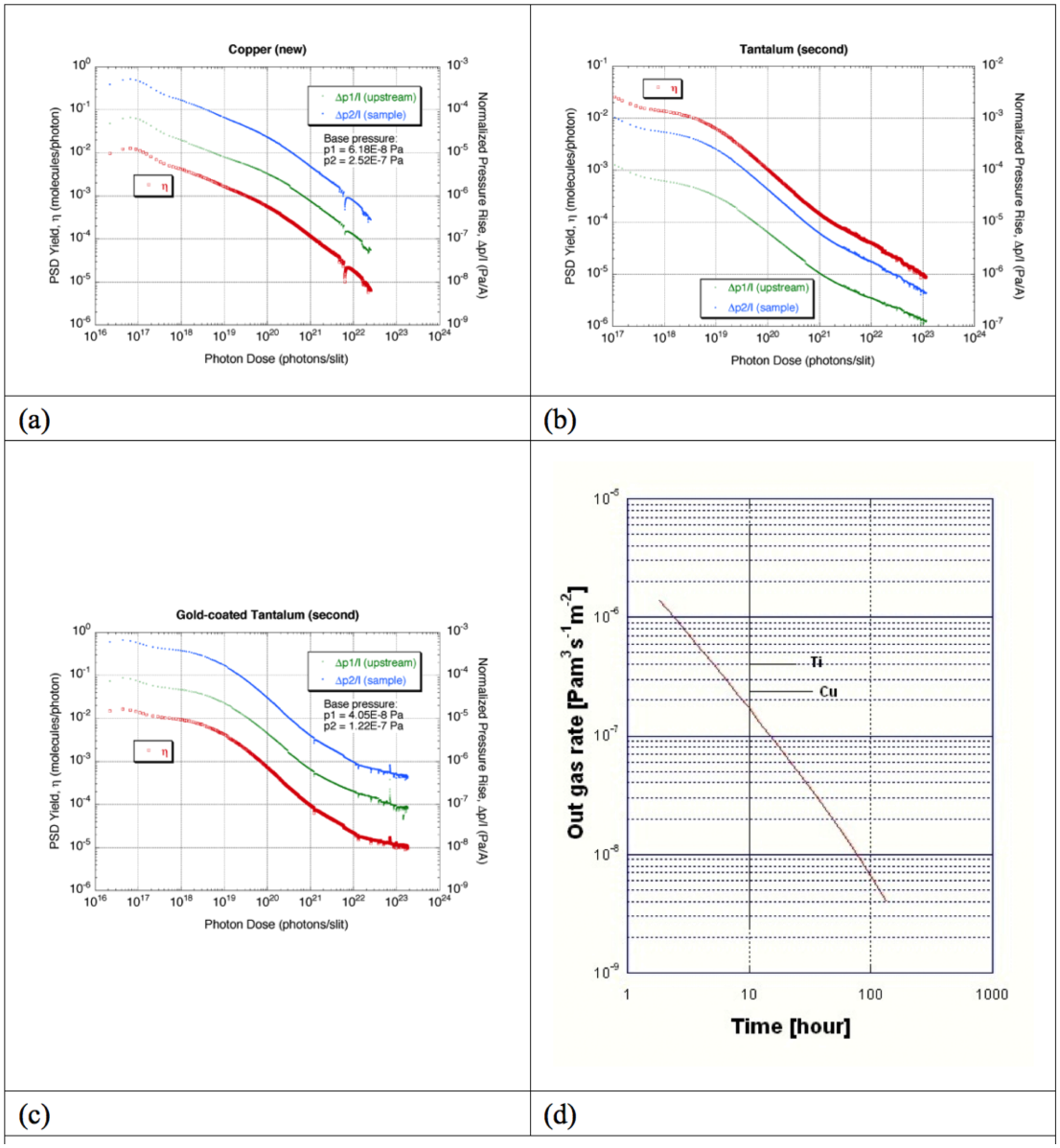

Figure 5.21: Outgassing data. (a) Photo-desorption coefficient of Cu. (b) Photo-desorption coefficient of Ta. (c) Photo-desorption coefficient of Au coat on Ta. (d) Thermal outgassing rate of Ta.

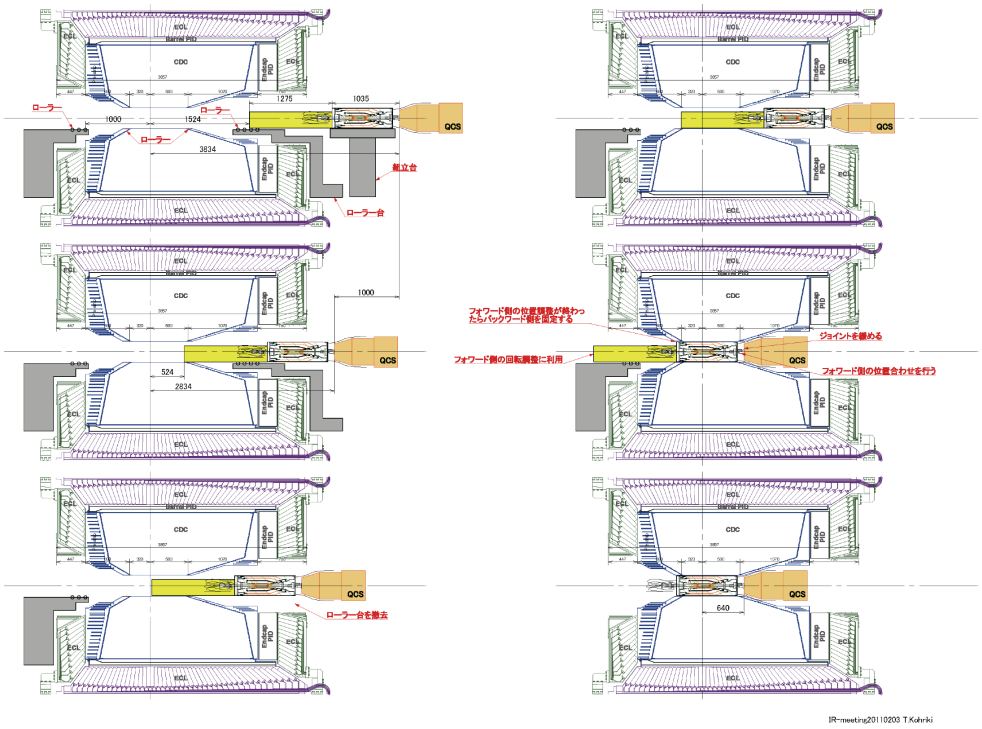

Figure 5.22: Baseline installation scenario. Start is left top, and end is right bottom.

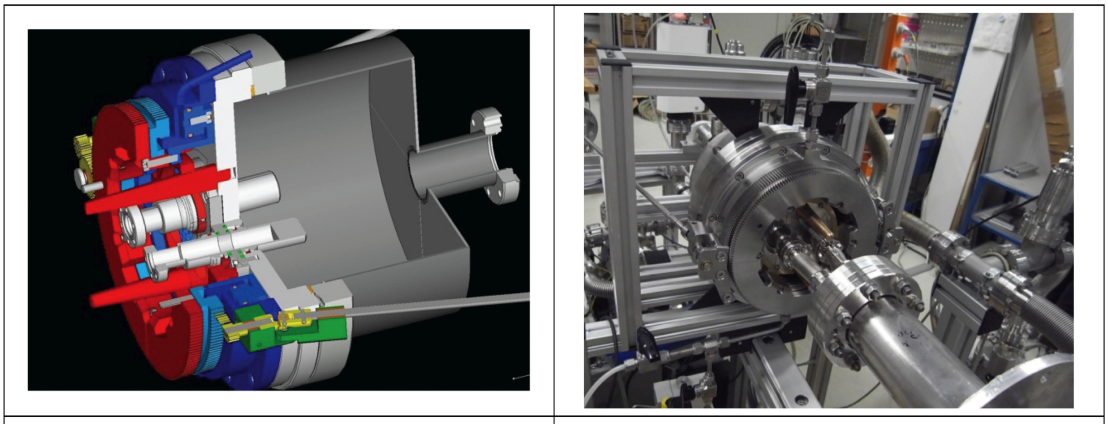

(a) (b)

Figure 5.23: RVC mechanism. (a) A cut view of a test mock-up. (b) The mock-up for vacuum test.

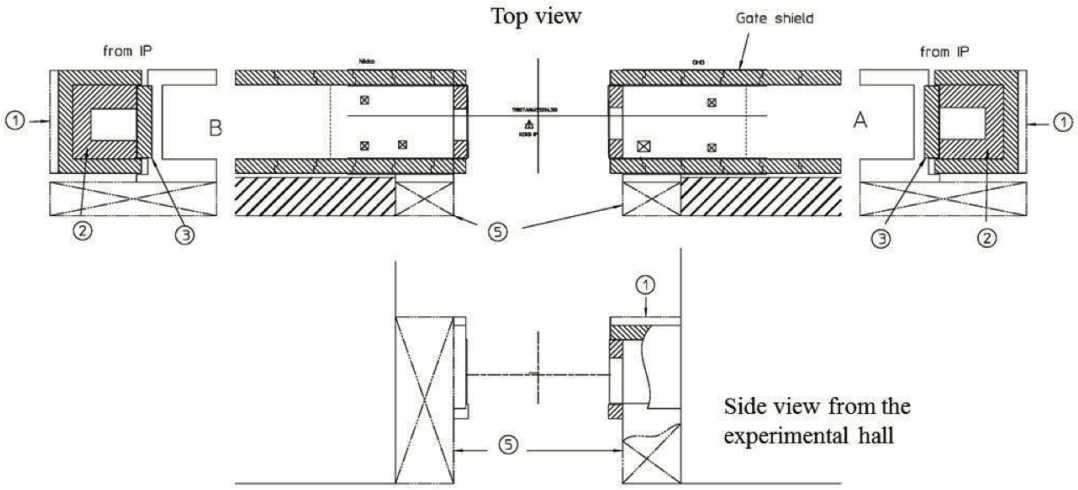

Figure 5.24: RVC mechanism. (a) A cut view of a test mock-up. (b) The mock-up for vacuum test.

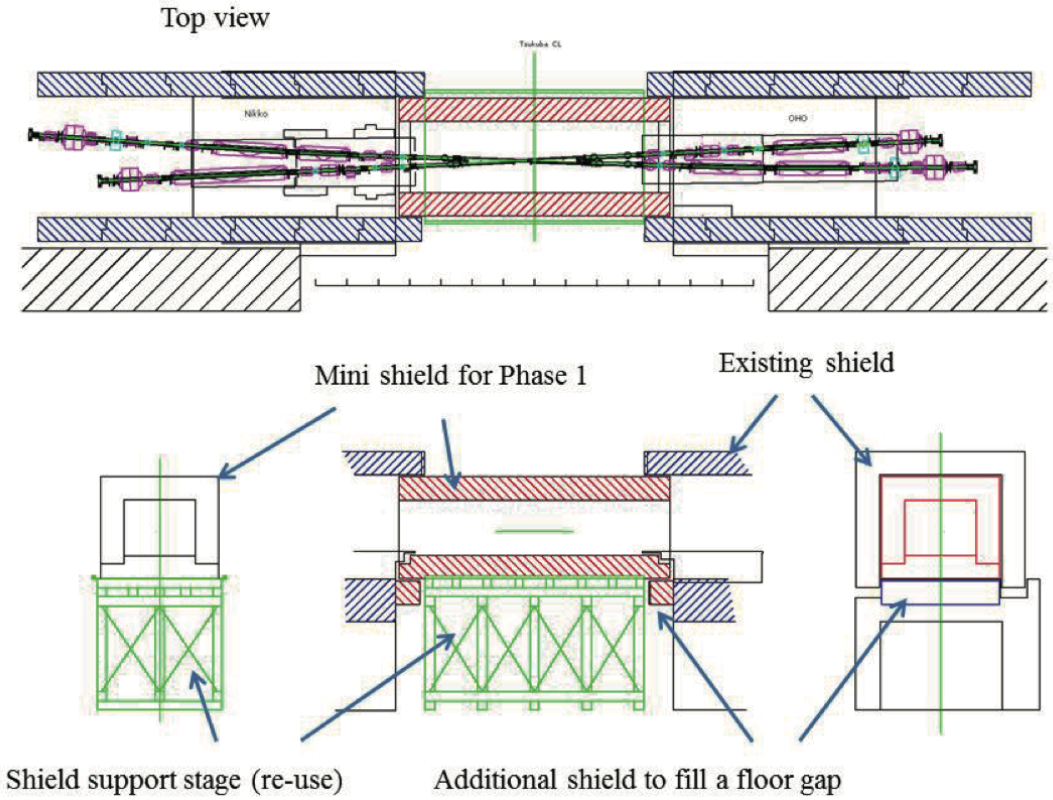

Figure 5.25: Phase 1 layout of the interaction region with concrete shield

The commissioning of the SuperKEKB starts from a vacuum scrubbing phase (Phase 1). The main purpose of the Phase 1 is the scrubbing of new LER beam pipes with synchrotron radiation to reduce the photo-desorption coefficient. In this phase, Belle II detector is out of the interaction region (in the roll-out position) and there are no final focus QCS magnets. Temporal Al beam pipes are set at the interaction point and the QCS location. A compact concrete shield covers these beam pipes. This shield keeps the experimental hall as a non-controlled area under the Phase 1 operational condition. Fig. 5.25 shows a layout of the interaction region during Phase 1.

5.7 Beam Background

With increased luminosity at SuperKEKB, we need to carefully estimate the beam background impact on Belle-II detector. If beam background exceeds the acceptable level, radiation might kill Si devices, fake hits might deteriorate detector resolution, and high occupancy might use up bandwidth of data acquisition path. Major sources of beam background at SuperKEKB are: beam-induced backgrounds sources(Touschek

scattering, beam-gas scattering), luminosity-dependent background sources (radiative Bhabha process, two-photon process), synchrotron radiation, and so on.

5.7.1 Beam background sources

- Touschek effect

  Touschek effect is an intra-bunch scattering between two beam particles in the same bunch [10]. The scattered particles with too little or too much energy start to deviate from the design orbit while they travel along the ring, and will finally be hi ting the beam pipe and generate electromagnetic showers. If the beam loss position is in the neighborhood of the Belle-II detector, the shower particles can reach the detector.

  At SuperKEKB, simple extrapolation using beam size parameter predicts that the beam background by Touschek effect will increase by factor of $\sim$20 compared to that of KEKB. However, it can be dramatically mitigated by movable collimators which can stop the deviated particles before they reach the interaction region.

  Horizontal collimators are installed at both inner and outer side of the beam orbit. Collimators are located at the positions where horizontal beta function or the dispersion becomes local-maximum. Collimator opening widths are selected to achieve good background mitigation and beam lifetime at the same time.

- Beam-gas effect

  Beam particles scatted by the residual gas atoms in the beam pipe are also deviated from the design orbit, like Touschek-scattered particles. Here we assume both Coulomb scattering and Bremsstrahlung scattering.

  The beam-gas scattering rate is proportional to the vacuum level and the beam current. At SuperKEKB, the beam currents will be $\sim$ 2 times higher than that of KEKB, and the vacuum level except for the interaction region will be the same level as KEKB. Therefore we have been expected the same order of magnitude (a few times higher) beam-gas background in the past publications [12]. However, our latest simulation study reveals that Coulomb scattering rate is higher by factor of $\sim$ 100 than that of KEKB, since IR beam pipe aperture is smaller and the maximum vertical beta function is larger.

  Beam-gas Coulomb background can be mitigated by vertical collimators, but the collimator half width should be very small (few mm), due to the Transverse Mode

Coupling (TMC) instability caused by the collimator. For more details, please refer [11].

In addition, slight misalignment of the vertical collimator can easily lead to significant increase of the background level. Therefore $sum\ 50\mu m$ precision for the movable collimator system is required.

- Radiative Bhabha process

  Gammas emitted from radiative Bhabha scattering by beam collisions travel straight to the downstream and interact with beam pipes or magnets. In these interactions, neutrons are copiously produced via the giant photo-nuclear resonance mechanism. Those neutrons scattered back to the detector is dangerous for the outermost KL and muon detectors (KLMs).

  Electrons or positrons lose energy after radiative Bhabha scattering by beam collision. In case of KEKB, since we employed the shared final quadrupole magnet scheme, downstream beam orbits go through off-center of the quadrupole magnets and therefore the spent beam particles were over-bent strongly. At SuperKEKB, we introduce individual final quadrupole magnet scheme, therefore spent beam particles are more likely to go through the interaction region without hitting the beam pipe. However, if they lose so much energy, they can still hit the beam pipe inside or near the Belle-II detector (typically particles below 2 GeV can be lost inside the detector), and generated shower particles can reach to the detector.

  Radiative Bhabha background is proportional to the luminosity. With 40 times higher luminosity at SuperKEKB, radiative Bhabha background is the most dominant background source, after the mitigation of T??o??u??s??c??h??e??k?? and beam-gas background by movable collimators.

- Two-photon process

  Low momentum electron-positron pairs produced via the two-photon process ($ee \to eeee$) by beam collision. This background source is important for the inner detectors. At SuperKEKB, the radius of the innermost detector is less than that of KEKB since we introduce the pixel detector close to the IP. The two-photon background rate increases roughly as $1/r^2$. Curling tracks might be dangerous, since they might hit the inner detectors many times while curling.

- Synchrotron radiation

  Synchrotron radiation photons are generated from the beam particles when the orbit is bent. It might penetrate beam pipe and reach the inner detectors. To

absorb the synchrotron radiations before they reach the inner detectors, the inner surface of the Beryllium beam pipe are coated with gold plate. The shape of IR beam pipe is carefully designed to avoid direct SR hits at the detector. The energy of SR which we are worring is from few keV to tens of keV.

- Other background sources

  Beam background during the injection is also important background source. We need to apply timing veto on the innermost detector, to achieve comfortable data acquisition rate.

  Beam-beam kick effect, the interaction of a beam bunch with the electric field of the other beam bunch at collision point, changes the beam shape to distorted distribution, not a Gaussian. This effect should be carefully taken into account, especially when estimating the halo effect on synchrotron radiation.

Simulation tools

For Touschek and beam-gas background, we use theoretical formulae [16] to generate distribution of scattered beam particle energy and direction. For radiative Bhabha background, we use BBBREM [13] generator. Generated particles are then tracked using SAD [15] code, until they are lost by hitting beam pipes. Then loss particles information is provided to Geant4 [17], and Geant4 takes care of simulating shower propagation and detector response.
2-photon background is generated by Diag36(BDK) [14] generator, and provided directly to Geant4. Synchrotron radiation is generated inside Geant4 framework, and simulated by Geant4.

Beam loss distribution

Figure 5.26 shows the beam loss distribution inside Belle-II detector, weighted by energy of lost beam particle. Particles lost by radiative Bhabha process are mainly less than 2 GeV, while Touschek and beam-gas particles are almost 4 GeV (positrons) or 7 GeV (electrons).
Table 5.13 summarizes the loss rates within $|z| < 4$ m. Radiative Bhabha components give dominant impact on the detector.

Impact on Belle-II detector

We simulate the impact of the beam background on the sub-detectors of Belle-II detector: PXD, SVD, CDC, TOP, ARICH, ECL, and KLM. By adding few more shielding

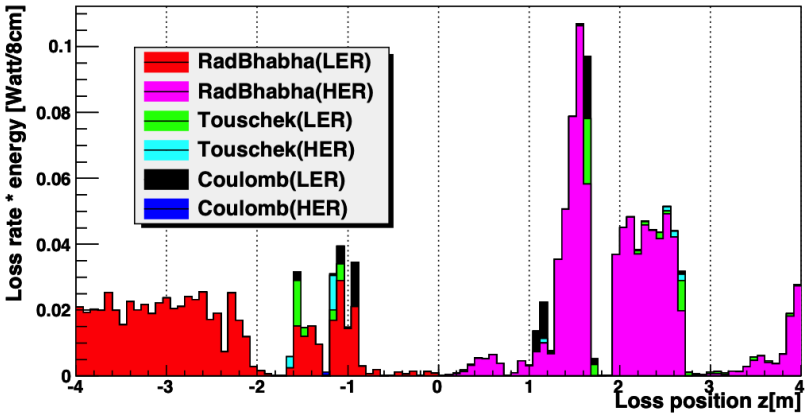

Figure 5.26: Beam loss distribution inside the Belle-II detector, weighted by beam particle energy.

	LER	HER
Radiative Bhabha	0.63 W	0.88 W
Touschek	0.07 W	0.02 W
Coulomb	0.07 W	0.001 W

Table 5.13: Beam loss rate inside the Belle-II detector, weighted by beam particle energy.

structure inside the detector, we have confirmed that the estimated background levels are acceptable for most of our sub-detectors, assuming 10 years of machine operation at full design luminosity:

- PXD/SVD occupancy are OK
- CDC wire hit rates are OK
- radiation dose on PXD/SVD chips, ECL crystals/diodes are OK
- neutron rate on CDC FPGA chips, ARICH HAPD sensors, and end-cap KLMs are OK

However, we found TOP PMT photocathode might not survive for 10 years at full design luminosity. We are planning to replace them with new PMTs, after few years of operation.
Validity of those simulation are confirmed by BEAST experiments prior to the start of physics runs. We install BEAST sensors to measure radiation levels inside the detector

during the machine comissioning period, to make sure we can safely install our Belle-II detectors. Details of BEAST experiments can be found elsewhere[18].

Bibliography

[1] N. Ohuchi et al., "Design of The Superconducting Magnets System for The SuperKEKB Interaction Region," WEODA1, Proceedings of NA-PAC2013, Pasadena, September 2013, pp. 759-761 (2013).

[2] [Y. Makida, *et al.*, "Development of a superconducting solenoid magnet system for the B-Factory detector (BELLE)," Advances in Cryogenic Engineering, Vol. 43A, 1998, pp. 221-228.

[3] H. Yamaoka et al., "Solenoid Field Calculation of the SuperKEKB Interaction Region," THPPD023, Proceedings of IPAC2012, New Orleans, May 2012, p. 3548 (2012).

[4] B. Parker et al., "Superconducting Corrector IR Magnet Production for SuperKEKB," THPBA07, Proceedings of NA-PAC2013, Pasadena, September 2013, pp. 1241-1243 (2013).

[5] B. Parker et al., "Direct Wind Superconducting Corrector Magnets for the SuperKEKB IR," IPAC12, New Orleans, LA, WEEPPB013, p. 1291 (2012).

[6] B. Parker, *et al.*, "BNL direct wind superconducting magnets", *IEEE Trans. on Appl. Supercond.*, Vol. 22, No. 3, 2012, 4101604.

[7] N. Ohuchi et al., "Design and Construction of the Proto-type Quadrupole Magnets for the SuperKEKB Interaction Region," THPBA04, Proceedings of NA-PAC2013, Pasadena, September 2013, pp. 1241-1243 (2013).

[8] N. Ohuchi et al., "Design and Construction of the Magnet Cryostats for the SuperKEKB Interaction Region," *IEEE Trans. on Appl. Supercond.*, Vol. 28, No. 3, 2018, 4003204.

[9] Z. Zong, N. Ohuchi, K. Tsuchiya, Y. Arimoto "Development of a compact HTS lead unit for the SC correction coils of the SuperKEKB final focusing magnet system", NIM PR-A 830, 2016, pp. 279-286.

[10] A. Piwinski, "The Touschek effect in strong focusing storage rings," physics/9903034.

[11] Y. Funakoshi, K. Ohmi, Y. Ohnishi, K. Kanazawa, Y. Suetsugu, H. Nakayama and H. Nakano, "Small-Beta Collimation at SuperKEKB to Stop Beam-Gas Scattered Particles and to Avoid Transverse Mode Coupling Instability," Conf. Proc. C **1205201**, 1104 (2012).

[12] T. Abe *et al.* [Belle-II Collaboration], "Belle II Technical Design Report," arXiv:1011.0352 [physics.ins-det].

[13] R. Kleiss and H. Burkhardt, "BBBREM: Monte Carlo simulation of radiative Bhabha scattering in the very forward direction," Comput. Phys. Commun. **81**, 372 (1994) [hep-ph/9401333].

[14] F. A. Berends, P. H. Daverveldt and R. Kleiss, "Monte Carlo Simulation of Two Photon Processes. 2. Complete Lowest Order Calculations for Four Lepton Production Processes in electron Positron Collisions," Comput. Phys. Commun. **40**, 285 (1986).

[15] http://acc-physics.kek.jp/SAD/sad.html

[16] Y. Ohnishi, T. Abe, T. Adachi, K. Akai, Y. Arimoto, K. Ebihara, K. Egawa and J. Flanagan *et al.*, "Accelerator design at SuperKEKB," PTEP **2013**, 03A011 (2013).

[17] S. Agostinelli *et al.* [GEANT4 Collaboration], "GEANT4: A Simulation toolkit," Nucl. Instrum. Meth. A **506**, 250 (2003).

[18] http://belleweb.pnnl.gov/forTDRreview/TDR-SLAC-13Dec8.pdf